

ORIGINAL RESEARCH

Open Access



# Pyrolytic synthesis of graphene-encapsulated zero-valent iron nanoparticles supported on biochar for heavy metal removal

Tharindu N. Karunaratne<sup>1</sup>, R. M. Oshani Nayanathara<sup>1</sup>, Chanaka M. Navarathna<sup>2</sup>, Prashan M. Rodrigo<sup>2</sup>, Rooban V. K. G. Thirumalai<sup>3</sup>, Charles U. Pittman Jr.<sup>2</sup>, Yunsang Kim<sup>1</sup>, Todd Mlsna<sup>2</sup>, Jilei Zhang<sup>1</sup> and Xuefeng Zhang<sup>1\*</sup> 

## Abstract

Biochar (BC)-supported graphene-encapsulated zero-valent iron nanoparticle composites (BC-G@Fe<sup>0</sup>) are promising engineering nanocomposites that can be used to scavenge heavy metal from wastewater. However, the production of BC-G@Fe<sup>0</sup> through carbothermal reduction using biomass as a carbon source remains challenging because of biomass pyrolysis complications. Here, we examined two carbothermal reduction routes for preparing BC-G@Fe<sup>0</sup> using bamboo as the carbon source. The first route impregnated Fe ions (Fe<sup>2+/3+</sup>) into unpyrolyzed bamboo particles initially, followed by carbonization at 600–1000 °C. This process produced BC-G@Fe<sup>0</sup> dominated by iron carbide (Fe<sub>3</sub>C), which led to low heavy metal removal efficiency (i.e., Cu<sup>2+</sup> capacity of < 0.3 mmol g<sup>-1</sup>). In the second route, bamboo particles were pyrolyzed (600 °C) to biochar first, followed by impregnating this biochar with Fe ions, and then carbonized at 600–1000 °C. This route produces zero-valent iron nanoparticles, which resulted in high heavy metal removal capacities (i.e., 0.30, 1.58, and 1.91 mmol g<sup>-1</sup> for Pb<sup>2+</sup>, Cu<sup>2+</sup>, and Ag<sup>+</sup>, respectively). The effects of carbonization temperature (600–1000 °C), iron source (i.e., iron nitrates, iron sulfate, ferrous chloride, and ferric chloride), and iron loading (5–40%) on the morphology, structure, and heavy metal ion aqueous uptake performance of BC-G@Fe<sup>0</sup> were also investigated. This study revealed the formation mechanisms of BC-G@Fe<sup>0</sup> through biomass carbothermal reduction, which could guide the application-oriented design of multifunctional iron-BC composites for water remediation.

## Highlights

- BC-G@Fe<sup>0</sup> nanocomposite was produced through two carbothermal reduction routes.
- The biomass impregnating-carbonizing route produced graphene-encapsulated iron carbide (Fe<sub>3</sub>C) nanoparticles.

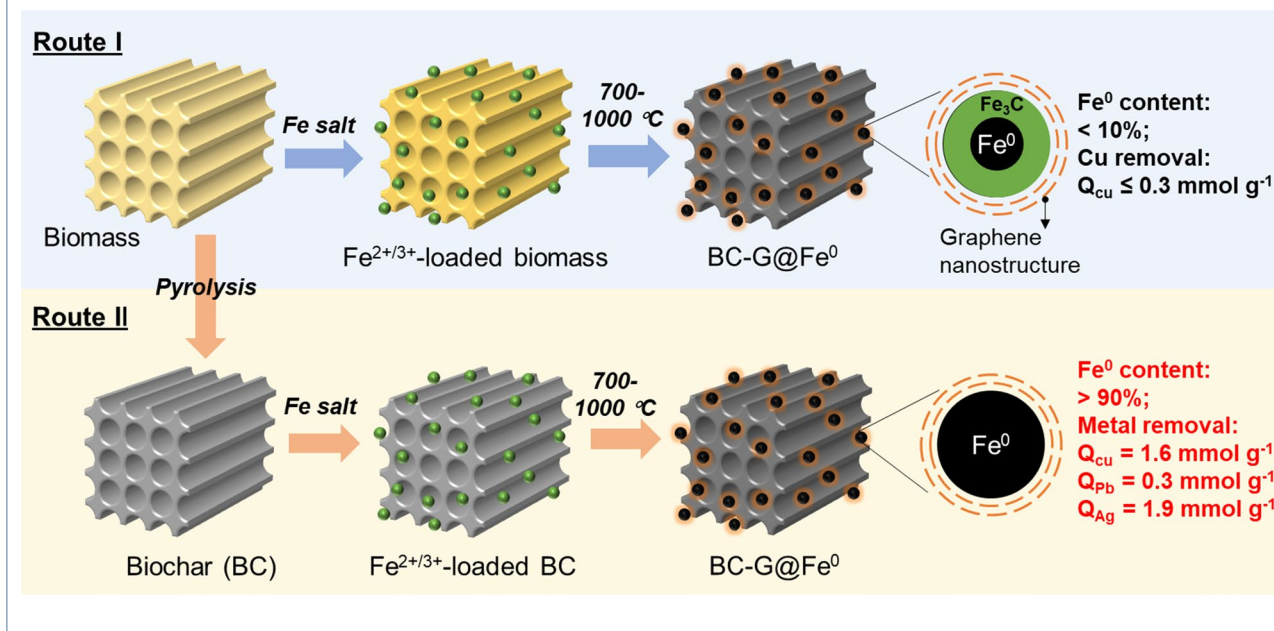
\*Correspondence: xz210@msstate.edu

<sup>1</sup> Department of Sustainable Bioproducts, Mississippi State University, Mississippi State, MS 39762, USA  
Full list of author information is available at the end of the article

- The pyrolyzing-biochar-impregnating-carbonizing route produced graphene-encapsulated nanoscale zero-valent iron particles.
- BC-G@Fe<sup>0</sup> nanocomposites exhibited good heavy metal ion removal performance.

**Keywords:** Bamboo, Biochar, Carbothermal reduction, Fe<sub>3</sub>C, Metallic iron, Heavy metal

### Graphical Abstract



## 1 Introduction

Heavy metal pollution is a global environmental issue that threatens 200 million people worldwide (Tchounwou et al. 2012). Heavy metals such as copper (Cu), lead (Pb), and silver (Ag) have devastating effects on humans (Wani et al. 2015). Cu<sup>2+</sup> is a toxic heavy metal usually discharged from mining, farming, and corrosion of pipes (Briffa et al. 2020; Samaraweera et al. 2022). Pb<sup>2+</sup> is the most toxic heavy metal originating from various sources such as leaded gasoline, water pipes, lead-based paint, battery recycling, etc. (Madduri et al. 2020). Ag<sup>+</sup> is a rare metal that has adverse effects on human and aquatic life. The anthropogenic sources of Ag<sup>+</sup> include emissions from smelting operations, cloud seeding, and photographic and electrical supplies (Eisler 1996).

Nanoscale zero-valent iron (nanoFe<sup>0</sup>) features a low reduction potential (E<sup>0</sup>) and high reactivity. It is a promising material for heavy metal immobilization from polluted water. Specifically, nanoFe<sup>0</sup> can capture heavy metal ions such as Pb<sup>2+</sup>, Cu<sup>2+</sup>, and Ag<sup>+</sup> with the E<sup>0</sup> higher than − 0.44 eV by reduction, sequestering them as solid metal particles (Zhang et al. 2021b). Moreover, Fe<sup>2+/3+</sup> ions released from nanoFe<sup>0</sup> dissolution can immobilize

heavy metals from wastewater solution through hydrolysis to iron hydroxide and co-precipitation (Zhang et al. 2021b). However, nanoFe<sup>0</sup> suffers agglomeration issues because of its ferromagnetic high surface area. Agglomeration reduces the nanoFe<sup>0</sup> surface area, which limits its mobility in polluted water, thereby reducing its water remediation performance (Huang et al. 2020; Jiao et al. 2019; Ng and Lim 2022). Depositing nanoFe<sup>0</sup> onto a high surface area carrier can alleviate the agglomeration. Carriers including clay, zeolite, metal–organic frameworks, graphene, and biochar (BC) have been used for nanoFe<sup>0</sup> dispersion (Asif et al. 2021; Bagheri et al. 2021; Ezzatah-madi et al. 2017; Florea et al. 2022; Li et al. 2018; Liu et al. 2019; Wang et al. 2019; Xing et al. 2020). BC is a low cost and effective candidate for dispersing nanoFe<sup>0</sup> because of its highly porous high surface area structure and many surface functional groups (Wang et al. 2019). BC-supported nanoFe<sup>0</sup> composite (BC-Fe<sup>0</sup>) has frequently been prepared by borohydride reduction of Fe<sup>2+/3+</sup> containing solutions (Yang et al. 2021). However, borohydrides are toxic and expensive, making large scale borohydride reduction a non-sustainable and less appealing BC-Fe<sup>0</sup> preparation route.

Recently, carbothermal reduction has been used to produce BC-Fe<sup>0</sup> for water remediation (Fan et al. 2020b; Jiang et al. 2021; Ma et al. 2021). Typical carbothermal reduction process impregnates iron salts or oxides into biomass precursors and heats at high temperatures (e.g., 600–800 °C) under oxygen-limited conditions. The biomass is converted to BC while iron salts or oxides are reduced to nanoFe<sup>0</sup> particles, which attach to biochar surfaces (Zhang et al. 2022b). Generally, both solid carbon and released pyrolysis gases (CH<sub>4</sub>, CO, H<sub>2</sub>) are the main reagents causing reduction to Fe<sup>0</sup> (Yan et al. 2018c). However, this carbothermal reduction process is uncontrollable because of the complex biomass pyrolysis complexity. The structure, morphology, crystallinity and size of the reduced iron are hard to regulate. For instance, direct carbothermal reduction of Fe(NO<sub>3</sub>)<sub>3</sub>-impregnated rice straw at 800 °C produces BC-Fe<sup>0</sup> dominated by nanoFe<sup>0</sup> particles, while hydrothermally assisted carbothermal reduction yields BC with distributed nanoFe<sup>0</sup>, FeO, and Fe<sub>2</sub>O<sub>3</sub> present (Yang et al. 2022). In contrast, the 800–1000 °C carbothermal reduction of ferric sulfate [Fe<sub>2</sub>(SO<sub>4</sub>)<sub>3</sub>]-impregnated rice husks yields Fe<sub>2</sub>O<sub>3</sub>, Fe<sub>3</sub>O<sub>4</sub>, and nanoFe<sup>0</sup> species (Liu et al. 2020). Moreover, iron carbides (Fe<sub>3</sub>C) generated in iron-assisted biomass pyrolysis products (Mun et al. 2015; Yan et al. 2018a; Zhang et al. 2018b), have often been overlooked or misinterpreted in the carbothermal production of BC-Fe<sup>0</sup> (Chen et al. 2021; Liu et al. 2020; Neeli and Ramsurn 2018; Yang et al. 2022). Furthermore, the role of Fe<sub>3</sub>C in water remediation is unclear. Studies have explored if Fe<sub>3</sub>C facilitates aqueous nitrate reduction (Lan et al. 2020). Fe<sub>3</sub>C is a stable compound that is not reactive to heavy metal water contaminants (Farzi et al. 2020). Additionally, the effect of the iron salts on the formation of BC-Fe<sup>0</sup> is still unclear. For example, carbothermal reduction of iron nitrate-impregnated sawdust at 800 °C gave BC-Fe<sup>0</sup> dominated by Fe<sub>3</sub>C (Mun et al. 2015) while carbothermal reduction of FeCl<sub>3</sub>-impregnated sawdust at the same temperature gave mainly nanoFe<sup>0</sup> (Jiang et al. 2019).

Our previous studies revealed that graphitic carbon nanostructures usually formed during the carbothermal reduction of iron oxides/salts impregnated into biomass (Yan et al. 2018b). These nanostructures are composed of graphene nanosheets and nanoribbons that form on the surface of iron species (nanoFe<sup>0</sup> and Fe<sub>3</sub>C) via carbon dissolution into the iron, graphene sheet formation and precipitation (Hunter et al. 2022) mechanisms. Layers of graphene sheets can encapsulate the iron particles to varying thicknesses. Recently, we have reported good heavy metal and nutrient removal from wastewater using BC-supported graphene-encapsulated nanoFe<sup>0</sup> (BC-G@Fe<sup>0</sup>) composites synthesized via in-situ carbothermal reduction

of Fe(NO<sub>3</sub>)<sub>3</sub> impregnated lignin (Zhang et al. 2021b). BC-G@Fe<sup>0</sup> composites were produced by the in-situ carbothermal reduction of FeCl<sub>3</sub>-impregnated sawdust and rice husk and used as persulfate activators for degrading 2,4-dichlorophenol (Zhang et al. 2021a) and acetaminophen (Zhuo et al. 2022), respectively. Biomass-derived BC-G@Fe<sup>0</sup> composites have attracted wide research for treating wastewater, but its synthesis mechanism is still unclear because of the biomass chemical heterogeneity and pyrolysis complexity. The formation of both Fe<sub>3</sub>C and graphitic nanostructures during iron catalytic graphitization of biomass is attributed to the carbonaceous compounds released during biomass pyrolysis. Thus, it remains a challenge to regulate the formation of Fe<sub>3</sub>C nanoparticles and specific graphitic nanostructures during the BC-G@Fe<sup>0</sup> production.

Considering these knowledge gaps, we sought to develop an effective BC-G@Fe<sup>0</sup> composite by carbothermal reduction to remove heavy metals. Hence, two carbothermal reduction routes to generate BC-G@Fe<sup>0</sup> were compared, i.e., the impregnating-carbonizing process and the pre-pyrolyzing-impregnating-carbonizing process (Fig. 1). The effects of the pre-pyrolyzing, carbonization temperature and iron source on the morphology, structure and heavy metal uptake performance of BC-G@Fe<sup>0</sup> were investigated. Specifically, model heavy metal removals of BC-G@Fe<sup>0</sup> were evaluated using aqueous Pb<sup>2+</sup>, Cu<sup>2+</sup>, and Ag<sup>+</sup> solutions. This revealed features of the pyrolytic synthesis mechanism of biomass-derived BC-G@Fe<sup>0</sup>. This knowledge base could guide the application-oriented design of multifunctional iron-BC composites for water remediation.

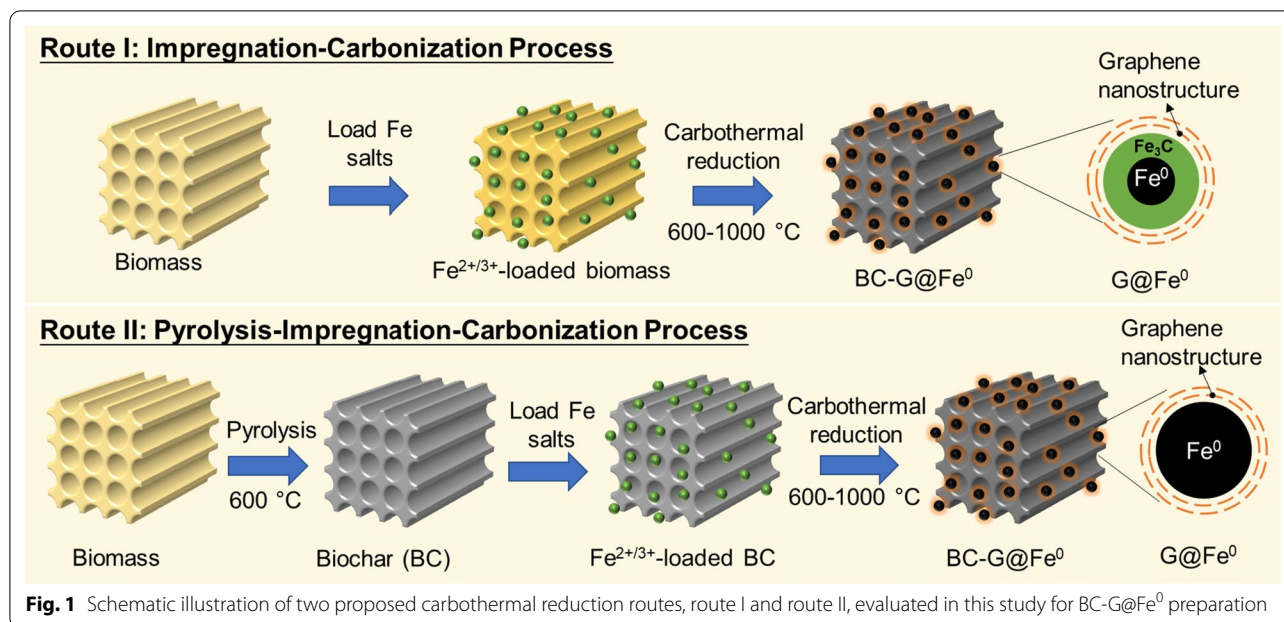
## 2 Experiments

### 2.1 Materials

Bamboo biomass was collected from a local farm (Starkville, MS, USA). Iron(II) chloride tetrahydrate (FeCl<sub>2</sub>·4H<sub>2</sub>O), iron(III) chloride (FeCl<sub>3</sub>), copper nitrate trihydrate [Cu(NO<sub>3</sub>)<sub>2</sub>·3H<sub>2</sub>O], lead nitrate [Pb(NO<sub>3</sub>)<sub>2</sub>] and hydrochloric acid (HCl) were purchased from Sigma Aldrich. Iron(III) nitrate nonahydrate [Fe(NO<sub>3</sub>)<sub>3</sub>·9H<sub>2</sub>O], and silver nitrate (AgNO<sub>3</sub>) were purchased from Alfa Aesar. Iron(II) sulfate heptahydrate [FeSO<sub>4</sub>·7H<sub>2</sub>O] was purchased from Acros Organics.

### 2.2 BC preparation

Dried bamboo strips (7% moisture content) with skin removed were ground into powders using a wood miller with a 180 μm mesh screen. Bamboo powders were pyrolyzed to BC in a tube furnace at 600 °C for 1 h



at a 50 °C min<sup>-1</sup> ramp rate under N<sub>2</sub> (1 L min<sup>-1</sup>). After washing with 1 M HCl and distilled water to remove ash, BC was oven-dried at 100 °C overnight. The dried BC was then ground to fine particles using a pestle.

### 2.3 Preparation of BC-G@Fe<sup>0</sup> by direct carbonization of Fe(NO<sub>3</sub>)<sub>3</sub> impregnated bamboo particles (route I)

Prior to BC-G@Fe<sup>0</sup> preparation, Fe(NO<sub>3</sub>)<sub>3</sub> was mixed with bamboo particles through a solvent impregnation method. Briefly, 3.6 g Fe(NO<sub>3</sub>)<sub>3</sub>·9H<sub>2</sub>O was mixed with 10 g bamboo (mass ratio of iron to the oven-dried bamboo is 5/100, labeled as 5%) in a beaker, followed by dispersing the mixture in 60 mL of deionized water. The mixture was then heated on a hot plate to ~60 °C while stirring for 2 h until all bamboo particles were saturated with the iron salt solution and had sank to the bottom of the beaker. Then this mixture was heated for another 2–6 h with stirring to evaporate the water, followed by oven drying at 103 °C overnight.

BC-G@Fe<sup>0</sup> was prepared through direct carbonization of Fe(NO<sub>3</sub>)<sub>3</sub>-impregnated bamboo particles at seven different targeted temperature levels, i.e., 600, 650, 675, 700, 800, 900, and 1000 °C, respectively. Specifically, 10 g of Fe(NO<sub>3</sub>)<sub>3</sub>-impregnated bamboo particles was loaded in two ceramic boats that were placed in the heating zone of a 2-inch (outer diameter) electric tubular furnace, followed by ramping (50 °C min<sup>-1</sup>) to a targeted temperature and holding for 1 h under a N<sub>2</sub> flow (1 L min<sup>-1</sup>). After cooling the furnace to room temperature over 2 h, the sample was removed. The products from direct carbonization were labeled as BC-G@Fe<sup>0</sup>-DX, where

“D” represents direct carbonization, and “X” represents the targeted carbonization temperature level used. The weights of products were measured using a digital balance (resolution 0.1 mg) giving the carbonization yield and allowing calculation of the iron content.

### 2.4 Preparation of BC-G@Fe<sup>0</sup> by carbonization of Fe salt-impregnated BC (route II)

Prior to BC-G@Fe<sup>0</sup> preparation, different iron salts were imbibed into BC (made at 600 °C, see Sect. 2.2) through a solvent impregnation method as described in Sect. 2.3. The type of iron salt used, Fe(NO<sub>3</sub>)<sub>3</sub>, FeCl<sub>2</sub>, FeCl<sub>3</sub>, and FeSO<sub>4</sub>, to impregnate BC was investigated with an iron loading of 15%. The effect of the carbonization temperature (e.g., 600, 700, 800, 900, and 1000 °C) was studied using FeCl<sub>2</sub> to impregnate BC, employing a mass ratio of 15% iron to BC. Iron loading was evaluated using FeCl<sub>2</sub>-impregnated BCs with iron loadings of 5%, 10%, 20%, 30%, and 40%.

BC-G@Fe<sup>0</sup> was then prepared by carbonization of Fe-impregnated BC particles at the predefined temperature using the same carbonization parameters (e.g., ramping rate and N<sub>2</sub> flow rate) described in Sect. 2.3. The products were labeled as BC-G@Fe<sup>0</sup>-X, where “X” represents the carbonization temperature used. The product weights were measured, and the iron contents were calculated (shown in Additional file 1: Table S1).

### 2.5 Adsorption study

Batch sorption experiments determined the Pb<sup>2+</sup>, Cu<sup>2+</sup>, and Ag<sup>+</sup> aqueous removal efficiency of BC-G@Fe<sup>0</sup>

samples synthesized from routes I and II. Briefly, BC-G@Fe<sup>0</sup> samples (50 mg) were dispersed in 40 mL solutions of the heavy metal at each concentration level evaluated. The mixtures were mechanically shaken vigorously for a predefined time at 25 °C. After completing metal uptake, the adsorbents were gravity filtered. The concentrations of Pb<sup>2+</sup> and Cu<sup>2+</sup> were determined by atomic absorption spectrophotometry (AAS). The Ag<sup>+</sup> concentration was determined using inductively coupled plasma mass spectrometry (ICP-MS). Copper, lead, and silver standardized solutions were prepared in the ranges of 0.5–20 mg L<sup>-1</sup>, 0.5–50 mg L<sup>-1</sup>, and 0.5–5 mg L<sup>-1</sup>, respectively. The uptake capacities of BC-G@Fe<sup>0</sup> were calculated using Eq. 1:

$$Q = (C_0 - C_f) \times V / m, \quad (1)$$

where Q (mg g<sup>-1</sup>) represents the metal amount (mg) adsorbed by 1 g of adsorbent; C<sub>0</sub> and C<sub>f</sub> are the initial and final metal concentrations (mg L<sup>-1</sup>) in the evaluated solution, respectively; V is the metal solution volume (L) and m is the adsorbent weight (g).

## 2.6 Characterization

X-ray diffraction (XRD) analysis was carried out to identify sample compositions using Cu-K $\alpha$  radiation over the 2 $\theta$  range of 20–80° with a Rigaku Ultima III X-ray diffractometer at a scanning speed of 1° min<sup>-1</sup> and step width of 0.05°. Field emission scanning electron microscopy (FESEM, JEOL-6500F) equipped with energy dispersive spectroscopy (EDS) was used to determine sample morphologies. BC-G@Fe<sup>0</sup> samples were placed on a conductive carbon adhesive tab that adhere to a stub. Then a 15 nm thick layer of Pt was sputter-coated to make the sample conductive before SEM analysis. The spot diameter of the Fe<sup>0</sup> nanoparticles in SEM images were calculated using ImageJ software. Transmission electron microscopy (TEM, JEOL-2100) equipped with EDS (Oxford X-max-80) was also used to investigate the surface morphology of BC-G@Fe<sup>0</sup> samples. TEM specimens were prepared by mixing approximately 10 mg of BC-G@Fe<sup>0</sup> samples with 5 mL ethanol first, followed by vortexing the suspension for 2 min. Then, a drop of the suspension was deposited onto a carbon film on a 300-mesh copper grid that was allowed to stand overnight under a vacuum before TEM analysis. BC-G@Fe<sup>0</sup> samples for specific surface area and pore volume measurements were degassed at 130 °C for 12 h before analyses by nitrogen sorption isotherms using a TriStar II PLUS (Micrometrics Instruments). The specific surface area, micropore and mesopore volumes were obtained according to N<sub>2</sub> adsorption isotherms using the nonlocal

density functional theory (NLDFT) method by assuming a slit pore model (Zhang et al. 2022a).

The surface elemental composition of BC-G@Fe<sup>0</sup> after heavy metal ion (Pb<sup>2+</sup>, Cu<sup>2+</sup>, and Ag<sup>+</sup>) removal tests were conducted using Thermo Scientific K-Alpha X-ray photoelectron spectroscopic system (XPS) equipped with a monochromatic X-ray source at 1486.6 eV (Al K $\alpha$  line). Briefly, 100 mg of BC-G@Fe<sup>0</sup> were added to 50 mL of heavy metal ion solution, and the mixture was then shaken mechanically (at a speed of 200 rpm min<sup>-1</sup>) for 15 min at 25 °C to characterize the surface region chemical structure of BC-G@Fe<sup>0</sup> after the uptake of heavy metal ions. The initial solution concentration and the initial pH for each of three metal ions were 500 mg L<sup>-1</sup> and 5, respectively. Following the removal tests, each mixture was first filtered, and the filtrate was then dried for 24 h at 80 °C under vacuum. The surface elemental composition of the dried filtrate was then investigated using XPS, high-resolution Pb, Cu, and Ag spectra. These were deconvoluted by assigning various peak counts using the Gaussian function in OriginPro 2021 software.

## 3 Results and discussion

### 3.1 BC-G@Fe<sup>0</sup> from direct carbonization of Fe(NO<sub>3</sub>)<sub>3</sub> impregnated bamboo particles (route I)

The direct carbonization of iron nitrate-impregnated bamboo biomass particles yields iron-containing nanoparticles supported on bamboo-derived biochar. The decomposition of iron nitrates and biomass occurs at the temperature below 500 °C where iron oxides and carbonaceous gases compounds are produced (Eq. 2). Iron oxides conversion to metallic iron will occur at a temperature above 500 °C under a reducing environment (Crane and Scott 2012), i.e., upon exposure to carbon, CO, H<sub>2</sub>, or CH<sub>4</sub> formed from further biomass thermal degradation (Eq. 2). Meanwhile, the dissolution of carbon atoms into iron particles above 500 °C generates iron carbides (e.g., Fe<sub>3</sub>C) (Eq. 3) (Liu et al. 2015). Both metallic iron and Fe<sub>3</sub>C nanoparticles were observed in XRD patterns of evaluated BC-G@Fe<sup>0</sup> (Fig. 2a). Specifically, a small amount of residual Fe<sub>2</sub>O<sub>3</sub> was found at 600 °C, while it was almost fully reduced to Fe<sup>0</sup> above 650 °C. At 675 °C, the carbon (002) peak was observed, indicating that the formation of graphitic carbon nanostructures probably was via the precipitation or extrusion of carbon from iron-carbon solid solutions (i.e.,  $\gamma$ -Fe and Fe<sub>3</sub>C) (Eqs. 4, 5) (Wirth et al. 2012). At 700 °C, diffraction intensities of both graphitic carbon and Fe<sub>3</sub>C increased, indicating that the formation of graphitic nanostructures was exceeded by formation of Fe<sub>3</sub>C. Further increasing the temperature from 700 to 1000 °C did not significantly change the phase composition of the products

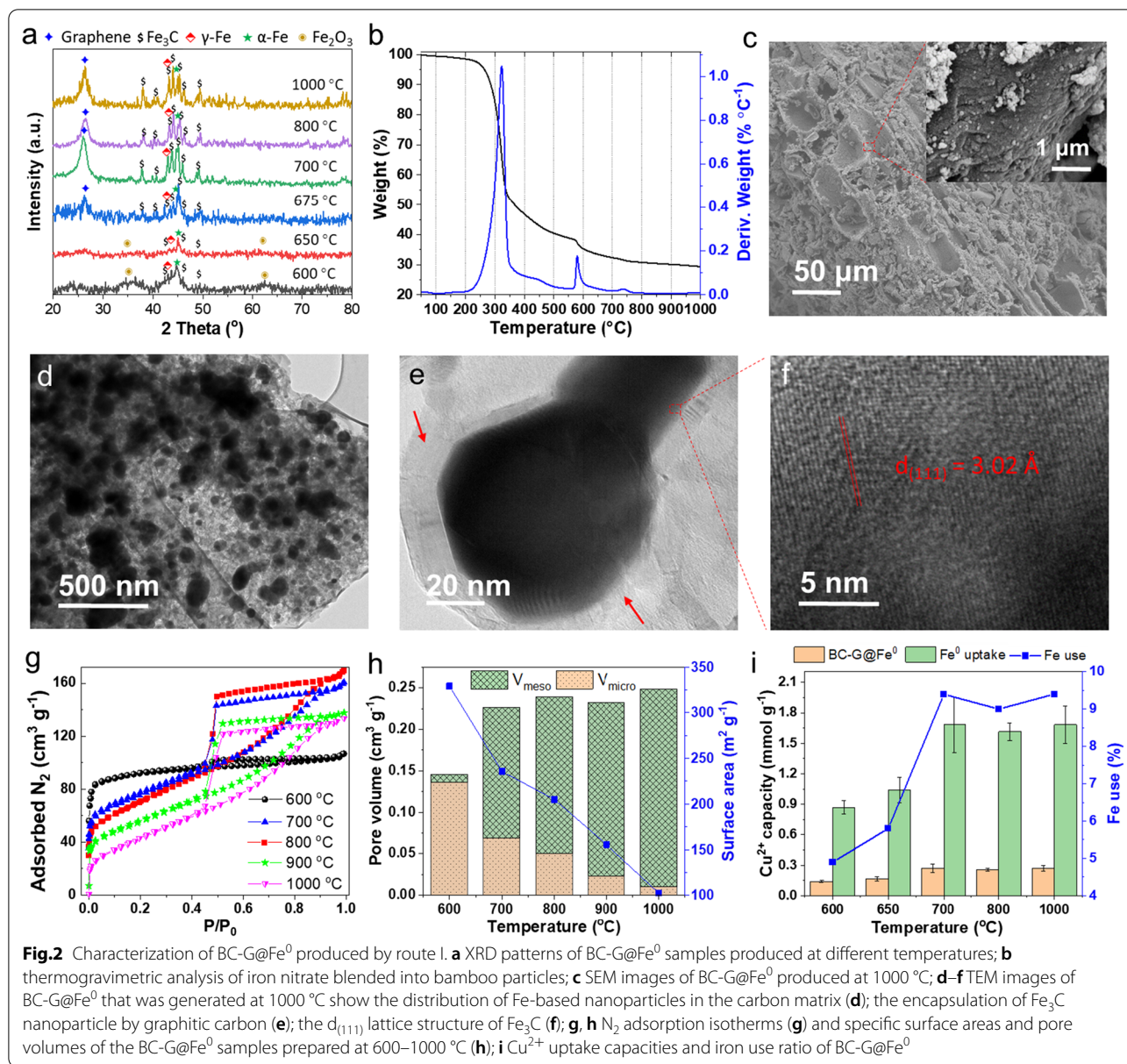
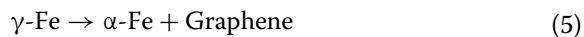
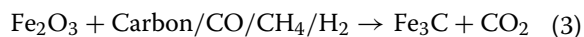
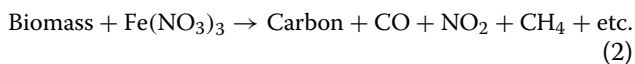


Figure 2b showed the thermogravimetric analysis of iron nitrate-impregnated bamboo particles. Three main weight loss peaks were observed on the weight derivative curve. The first peak centered at 330 °C occurs with approximately a 50% mass loss, which corresponds to the thermal degradation of bamboo. The second peak centered at 580 °C was related to the reduction of Fe<sub>2</sub>O<sub>3</sub> to Fe<sup>0</sup> and Fe<sub>3</sub>C nanoparticles. The third peak centered at 740 °C can be attributed to iron catalytic dehydrogenative BC carbonization and formation of graphene nanostructures. Iron-impregnated bamboo particles carbonized at 1000 °C exhibited a porous structure with many iron-based nanoparticles on their surfaces (Fig. 2c). TEM observations showed that these

iron-based nanoparticles with diameters less than 200 nm were embedded in an entangled graphitic nanoribbon and nanosphere network (Fig. 2d). High magnification TEM images indicated the iron-based (e.g., Fe<sub>3</sub>C and Fe<sup>0</sup>) nanoparticles had a core-shell structure consisting mostly of an iron-based nanoparticle cores that were shelled (covered) with 5–10 nm thick graphene layered nanostructures (Fig. 2e). Fe<sub>3</sub>C, which may be formed by carbon dissolving into α-Fe (Eq. 6), was also discovered in the outer layer of these nanoparticles (Fig. 2f). Thus, we postulated that nanoG@Fe<sup>0</sup> from direct carbonization consisted of a tertiary structure with the outer graphene surrounding layered nanostructured shell. The middle layer was Fe<sub>3</sub>C and

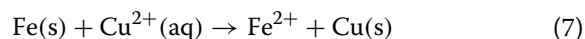
the core was nanoFe<sup>0</sup> (Fig. 1), as previously reported (Yan et al. 2013, 2019). Equations (2)–(6) express the general reaction features of the entire process.



The surface area and pore size of directly carbonized BC-G@Fe<sup>0</sup> samples were determined by N<sub>2</sub> adsorption isotherms (Fig. 2g). At 600 °C, the N<sub>2</sub> isotherms exhibited a typical Type Ia shape with an H4 hysteresis loop, indicating their microporous structure (Thommes et al. 2015). At 700 °C, N<sub>2</sub> isotherms showed the Type IVa shape with an H2 hysteresis loop, suggesting a developing mesoporous structure with some bottle-neck-shaped mesopores (Thommes et al. 2015). At temperatures of 700–1000 °C, the N<sub>2</sub> isotherms of BC-G@Fe<sup>0</sup> products showed the Type IVa shape with an H2 hysteresis loop, suggesting they all had bottle-neck-shaped mesoporous structures (Thommes et al. 2015). The microspore volume of BC-G@Fe<sup>0</sup> samples, made from 600 to 1000 °C, decreased from 0.138 to 0.010 cm<sup>3</sup> g<sup>-1</sup>. As a result, the specific surface area dropped from 329.1 to 102.5 m<sup>2</sup> g<sup>-1</sup> (Fig. 2h). However, the mesopore volume rose from 0.010 to 0.248 cm<sup>3</sup> g<sup>-1</sup>. This microporous-to-mesoporous transition with increasing temperature was related to the iron catalytic formation of graphene nanostructures. Specifically, the increase of temperature facilitated graphitic nanostructure (mainly mesoporous graphene nanoribbon and nanosphere) formation (Thompson et al. 2015) as indicated in XRD pattern (Fig. 2a). Moreover, the mobility of iron/iron carbide nanoparticles was increased at higher temperatures, this might also lead to reactive etching of microporous carbon and conversion of micropores to mesopore.

This BC-G@Fe<sup>0</sup> obtained from route I was used for Cu<sup>2+</sup> removal via batch adsorption tests, as shown in Fig. 2i. The Cu<sup>2+</sup> removal by BC-G@Fe<sup>0</sup> occurs mainly through a two-electron reduction reaction of Cu<sup>2+</sup> to Cu (Eq. 7). The Cu<sup>2+</sup> removal capacity is independent of the sample's surface area but dependent on the availability of the iron phases. As carbonization temperature rose from 600 to 700 °C, Cu<sup>2+</sup> removal capacity (Q<sub>Cu</sub>) increased from 0.14 to 0.27 mmol g<sup>-1</sup>, despite 50% decrease of surface area. This took place because Fe<sub>2</sub>O<sub>3</sub> was reduced to metallic iron nanoparticles, as illustrated in Fig. 2a.

More Fe<sup>0</sup> enhanced Cu<sup>2+</sup> removal by reducing more Cu<sup>2+</sup> to Cu<sup>0</sup> by Fe<sup>0</sup> oxidation. Increasing the carbonization temperature from 700 to 1000 °C did not change the Cu<sup>2+</sup> uptake capacity. This agrees with XRD scans showing BC-G@Fe<sup>0</sup> produced between 700 and 1000 °C have similar iron phase compositions. Theoretically, 1 mol of the metallic zero-valent iron nanoparticle can uptake 1 mol of Cu<sup>2+</sup> ions from an aqueous solution, and the corresponding uptake theoretical capacity (Q<sub>T-Cu</sub>) is 17.86 mmol g<sup>-1</sup>.

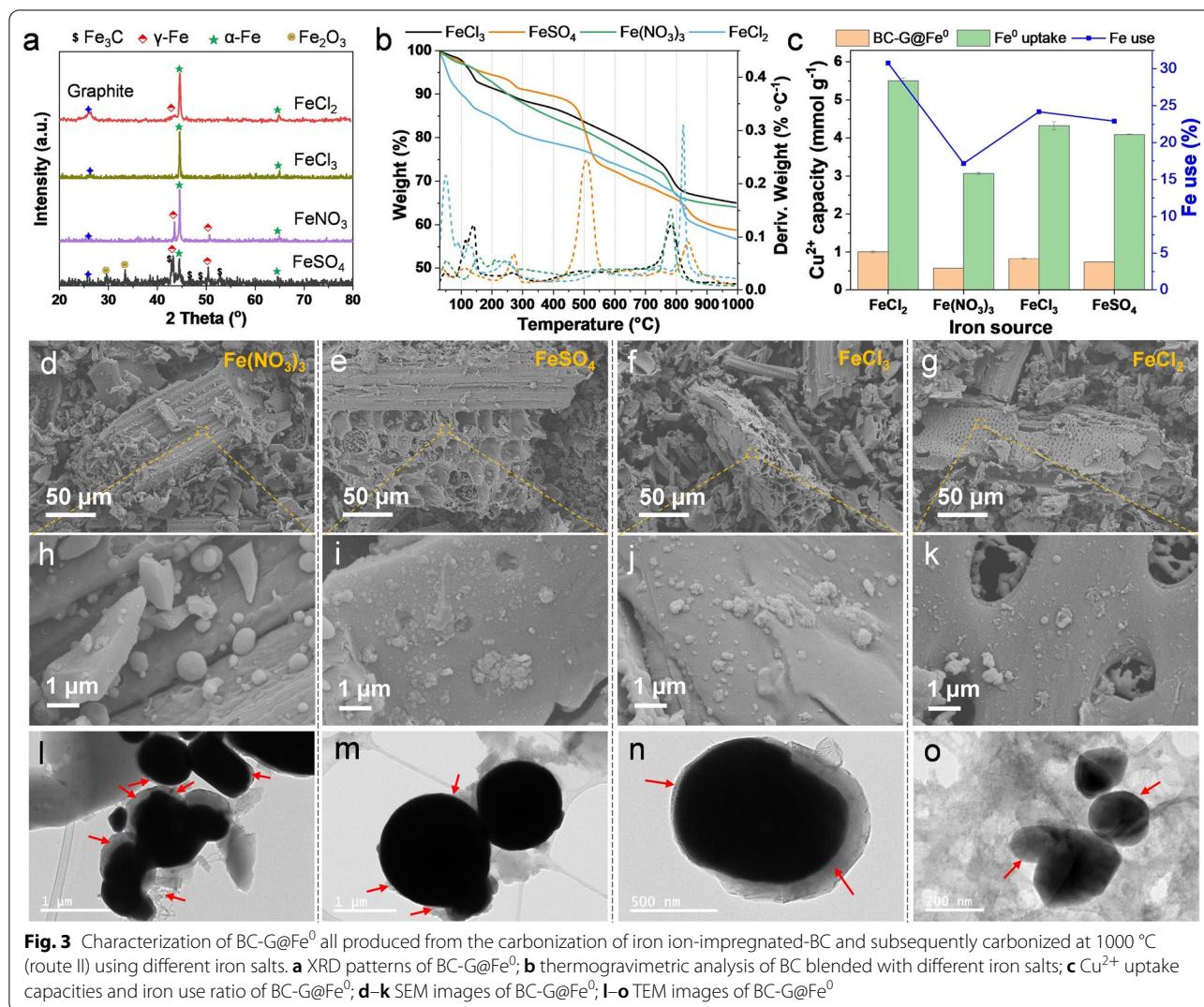


To evaluate the efficiency of direct carbonization of biomass/iron salt mixture (route I) for Fe<sup>0</sup> production and its heavy metal removal efficiency, we proposed two new parameters, namely iron uptake capacity (Q<sub>Fe-Cu</sub>) of Cu<sup>2+</sup> and iron use ratio. Briefly, Q<sub>Fe-Cu</sub> is calculated by dividing the Q<sub>Cu</sub> by its iron content, and Fe use ratio is calculated by Q<sub>Fe-Cu</sub> divided by Q<sub>T-Cu</sub>. The detailed calculation steps for Q<sub>T-Cu</sub>, Q<sub>Fe-Cu</sub>, and Fe use ratio were shown in Supporting information. As shown in Fig. 2i, as carbonization temperature rose from 600 to 700 °C, Q<sub>Fe-Cu</sub> increased from 0.87 to 1.69 mmol g<sup>-1</sup> and remained at ~1.65 mmol g<sup>-1</sup> between 700 and 1000 °C. Similarly, the Fe use ratio increased from 4.9 to 9.4% as the temperature increased from 600 to 700 °C and remained at ~9.4% thereafter. This low Fe use ratio was expected because Fe<sub>3</sub>C nanoparticles were dominant in BC-G@Fe<sup>0</sup> products produced by direct carbonization (Fig. 2a). Only small amounts of nanoFe<sup>0</sup> were present in BC-G@Fe<sup>0</sup> that were tightly wrapped by both graphene layer and Fe<sub>3</sub>C shells (Fig. 2a, e). Fe<sub>3</sub>C did not reduce Cu<sup>2+</sup>.

## 3.2 BC-G@Fe<sup>0</sup> from carbonization of Fe-impregnated BC (route II)

### 3.2.1 Effect of iron catalyst type

Fe<sub>3</sub>C lowered the Fe use ratio for Cu<sup>2+</sup> uptake. To eliminate the formation of Fe<sub>3</sub>C and increase the nanoFe<sup>0</sup> production in the carbonization products, bamboo particles were initially pyrolyzed at 600 °C for 1 h to make BC and remove carbonaceous gases (e.g., CH<sub>4</sub>, CO, etc.) in this first production stage without any Fe<sup>2+/3+</sup> impregnation. The bamboo-based BC particles produced were subsequently impregnated with iron salts and then further pyrolytically carbonized at 1000 °C to generate BC-G@Fe<sup>0</sup>. As depicted in XRD analysis in Fig. 3a, this suppressed the formation of Fe<sub>3</sub>C. These BC-G@Fe<sup>0</sup> products contained mostly metallic iron nanoparticles (i.e., α-Fe and γ-Fe). Specifically, carbonizing FeCl<sub>2</sub> and FeCl<sub>3</sub> impregnated in bamboo, only after it was converted to BC at 600 °C, produced mostly α-Fe nanoparticles. Carbonizing Fe(NO<sub>3</sub>)<sub>3</sub> impregnated BC yielded both α-Fe and γ-Fe nanoparticles. However, carbonizing FeSO<sub>4</sub>



impregnated BC yielded  $\alpha$ -Fe,  $\gamma$ -Fe, some Fe<sub>3</sub>C nanoparticles, as well as Fe<sub>2</sub>O<sub>3</sub> nanoparticles that were probably generated from the air passivation of  $\alpha$ -Fe and/or  $\gamma$ -Fe nanoparticles. The furnace was cooled to room temperature before the product was exposed to O<sub>2</sub>. Additionally, the carbon (002) diffraction peak was also observed in their XRD patterns (Fig. 3a).

Thermogravimetric analyses of bamboo BC are shown in Fig. 3b. Three main weight loss stages were observed. Briefly, the first stage occurred at temperatures of 50–250 °C and was related to loss of free bamboo moisture and decomposition of hydrated iron salts. The second stage occurring between 250 and 700 °C corresponded to the thermal degradation of iron salts. The third stage occurred above 700 °C and was attributed to the reduction of iron oxides and the formation of BC-G@Fe<sup>0</sup>.

Surface area and pore-size characterizations of BC-G@Fe<sup>0</sup> performed by N<sub>2</sub> adsorption experiments are displayed in Additional file 1: Fig S1. The specific surface areas of BC-G@Fe<sup>0</sup> samples made by route II were only between 2 and 20 m<sup>2</sup> g<sup>-1</sup>. This was much lower than the BC-G@Fe<sup>0</sup> samples produced from route I (i.e., 102.5–329.1 m<sup>2</sup> g<sup>-1</sup>). Despite their low surface areas, Cu<sup>2+</sup> uptake capacities (Q<sub>Cu</sub>) of BC-G@Fe<sup>0</sup> particles obtained from route II ranged from 0.57 to 1.01 mmol g<sup>-1</sup> (Fig. 3c). This was significantly higher than that of BC-G@Fe<sup>0</sup> samples obtained in route I (Fig. 2i), supporting our hypothesis that Fe<sub>3</sub>C formed at the expense of Fe<sup>0</sup> nanoparticles reduced heavy metal uptake. FeCl<sub>2</sub>-derived BC-G@Fe<sup>0</sup> exhibited the highest Q<sub>Cu</sub> of 1.00 mmol g<sup>-1</sup>, followed by FeCl<sub>3</sub>-derived BC-G@Fe<sup>0</sup> (0.82 mmol g<sup>-1</sup>), FeSO<sub>4</sub>-derived BC-G@Fe<sup>0</sup> (0.73 mmol g<sup>-1</sup>), and Fe(NO<sub>3</sub>)<sub>3</sub>-derived BC-G@Fe<sup>0</sup> (0.57 mmol g<sup>-1</sup>).

To elucidate the reasons for the differences in  $Q_{Cu}$ , the morphologies of BC-G@Fe<sup>0</sup> were obtained from route II using different iron salts. Uniform distribution of iron-based nanoparticles was formed on the surfaces of all samples (Fig. 3d–k). Importantly, the sizes of iron-based nanoparticles varied with the iron salts used. Specifically, Fe(NO<sub>3</sub>)<sub>3</sub>-derived BC-G@Fe<sup>0</sup> exhibited the largest Fe-based nanoparticles with the average diameter of 439 nm (measured by ImageJ, as shown in Additional file 1: Fig. S3). These were followed by FeSO<sub>4</sub>-derived BC-G@Fe<sup>0</sup> (average diameter of 171 nm, Additional file 1: Fig. S3), FeCl<sub>3</sub>-derived BC-G@Fe<sup>0</sup> (average diameter of 135 nm, Additional file 1: Fig. S3), and FeCl<sub>2</sub>-derived BC-G@Fe<sup>0</sup> (average diameter of 97 nm, Additional file 1: Fig. S3). Generally, nanoFe<sup>0</sup> particles with large sizes are less effective for heavy metal uptake because (1) heavy metal precipitates and (2) iron oxides formed on the surfaces. These increasingly prevent effective electron transfer from the nanoFe<sup>0</sup> core to heavy metal ions. Thus, a larger fraction of Fe<sup>0</sup> in the larger particles remains unoxidized. Thus, Fe(NO<sub>3</sub>)<sub>3</sub>-derived BC-G@Fe<sup>0</sup> exhibits the lowest  $Q_{Cu}$  while FeCl<sub>2</sub>-derived BC-G@Fe<sup>0</sup> exhibits the highest  $Q_{Cu}$ . In comparison with FeCl<sub>3</sub>-derived BC-G@Fe<sup>0</sup>, FeSO<sub>4</sub>-derived BC-G@Fe<sup>0</sup> contains more Fe<sub>3</sub>C, causing a lower  $Q_{Cu}$ .

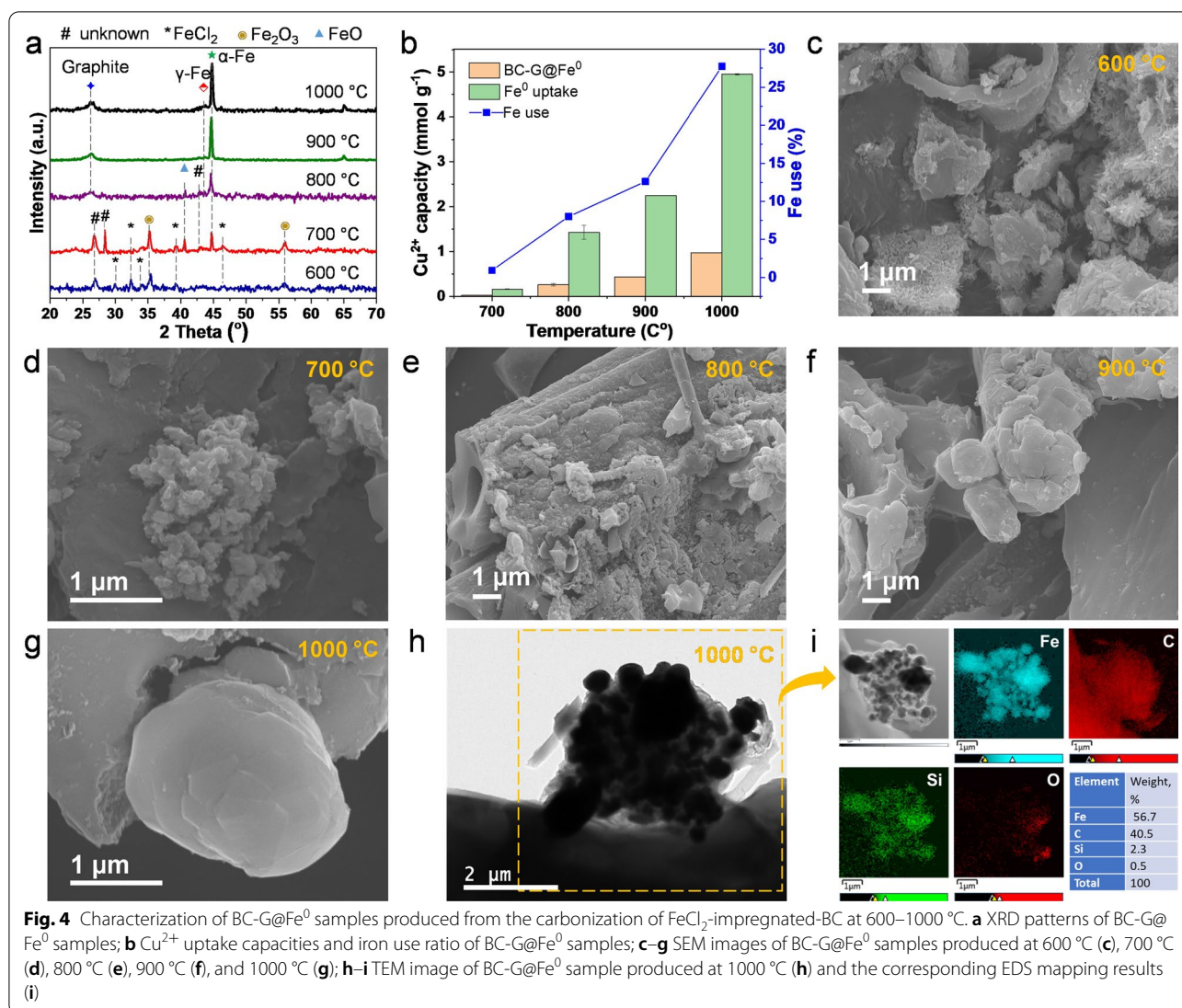
The morphology and structure of G@nanoFe<sup>0</sup> particles in BC-G@Fe<sup>0</sup> were studied by TEM (Fig. 3l–o). Individual particles display core–shell structures composed of metallic iron nanoparticle cores (nanoFe<sup>0</sup>, dark color portion) and a graphene nanoribbon shell (light color portion and labeled by red arrows). Note that the graphene nanoribbon encapsulations on nanoFe<sup>0</sup> surfaces are not perfect and homogeneous, i.e., some surfaces have thick graphene nanoribbons. Graphene growth on iron surfaces is crystal-structure dependent (Liu et al. 2012; Vinogradov et al. 2017), i.e., the (100) iron plane is more favorable for graphene formation. Graphene nanoribbons prevent further aggregation of nanoFe<sup>0</sup> particles by preventing direct Fe<sup>0</sup>/Fe<sup>0</sup> contact. These shells also increase nanoFe<sup>0</sup> particle stability by reducing their exposed surface area to other agents.

### 3.2.2 Effect of carbonization temperature

The effects of temperature and iron loading during the production of BC-G@Fe<sup>0</sup> were studied by selecting FeCl<sub>2</sub> as the iron source and carbonizing different loadings at 600–1000 °C. Figure 4a shows the XRD patterns of FeCl<sub>2</sub> impregnated BC, which then was carbonized at 600–1000 °C for 1 h (route II). At 600 °C, FeCl<sub>2</sub> was partly converted to Fe<sub>2</sub>O<sub>3</sub>, but nanoFe<sup>0</sup> was not formed. At 700 °C, FeO and α-Fe were formed due to the carbothermal reduction of Fe<sub>2</sub>O<sub>3</sub>, but FeCl<sub>2</sub> and Fe<sub>2</sub>O<sub>3</sub> predominated. At 800 °C,

the α-Fe diffraction peak dominated in the XRD pattern, and two small peaks corresponding to graphite and γ-Fe diffractions were observed, suggesting graphene-encapsulated iron nanoparticles had formed. However, a small FeO diffraction was still visible, indicating the carbothermal reduction to Fe<sup>0</sup> was not completed. At temperatures above 900 °C, carbonization product XRD patterns showed only α-Fe, γ-Fe, and graphite, completing the carbothermal reduction of iron oxides/chlorides. Moreover, higher γ-Fe and graphite diffraction intensities were observed in the BC-G@Fe<sup>0</sup> produced at 1000 °C.

$Q_{Cu}$  values exhibited significant increases from 0.02 to 0.98 mmol g<sup>-1</sup> upon increasing carbonization temperature from 700 to 1000 °C (Fig. 4b). The low Cu<sup>2+</sup> uptake capacities at 600 and 700 °C resulted from the small amount of nanoFe<sup>0</sup> formed. Carbonizing at 900 °C increased the Cu<sup>2+</sup> uptake capacity from 0.02 to 0.44 mmol g<sup>-1</sup>, because Fe<sup>0</sup> formation rose during the carbothermal reduction. Carbonization at 1000 °C doubled the Cu<sup>2+</sup> uptake capacity (0.98 mmol g<sup>-1</sup>), but the XRD patterns did not show many differences between these two samples. SEM characterization found (Fig. 4c, d), nanoparticle clusters were formed on the BC surfaces at 600 and 700 °C, which were nanoparticle clusters of iron oxides/chlorides confirmed by SEM-EDS mapping (Additional file 1: Figs. S4, S5). Higher temperatures promoted the decomposition and reduction of iron oxides/chlorides to iron. The Fe/Cl and Fe/O element ratios rose. BC-G@Fe<sup>0</sup> had a rough surface at 800 °C (Fig. 4e), attributed to etching of biochar from the carbothermal reduction. At 900 °C, nanoparticle clusters were observed on the surface of the BC (Fig. 4f). SEM-EDS mapping indicated the clusters consisted mostly of iron and carbon (Additional file 1: Fig. S6). At 1000 °C, micron-sized carbon/iron composite particles were observed in BC-G@Fe<sup>0</sup> (Fig. 4g and Additional file 1: Fig. S7, SEM-EDS mapping). The high-resolution TEM image (Fig. 4h) and EDS mapping (Fig. 4i) revealed nanoFe<sup>0</sup> particles were encapsulated by graphitic carbon, which agree with the XRD results. We previously reported that graphitic carbon coatings protect the core nanoFe<sup>0</sup> from oxygen passivation and enhances its heavy metal uptake efficiency (Zhang et al. 2021b). SEM-EDS revealed that oxygen was still present in carbon/iron composites synthesized at 900 °C and 1000 °C, suggesting surface oxidation of unprotected nanoFe<sup>0</sup> particles occurred. Specifically, the iron to oxygen atomic ratio of the 900 °C-derived BC-G@Fe<sup>0</sup> (Fe:O = 0.9:1) was lower than those formed at 1000 °C (Fe:O = 1.5:1), implying nanoFe<sup>0</sup> formed at 900 °C had a thinner protection layer and suffered more oxidation. This agrees with high intensity γ-Fe and graphitic XRD diffraction peaks of 1000 °C-derived BC-G@Fe<sup>0</sup>, confirming higher temperature facilitates the formation



of graphitic carbon encapsulations of iron nanoparticle (Zhang et al. 2018a).

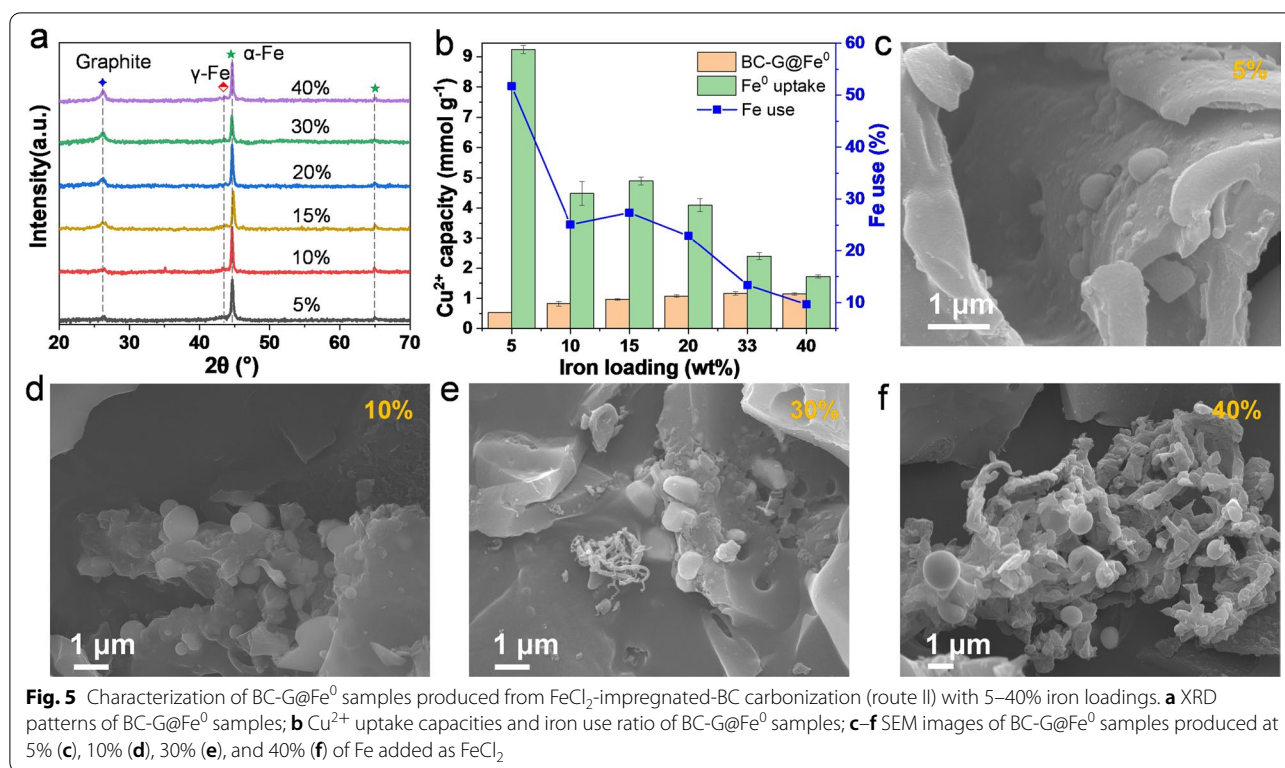
### 3.2.3 Effect of iron loading

The effect of iron loading on the structure, morphology and Cu<sup>2+</sup> uptake of BC-G@Fe<sup>0</sup> samples obtained at 1000 °C, were investigated. All XRD patterns of BC-G@Fe<sup>0</sup> samples had α-Fe, γ-Fe, and graphite diffraction peaks (Fig. 5a). The Q<sub>Cu</sub> of BC-G@Fe<sup>0</sup> increased from 0.53 to 1.14 mmol g<sup>-1</sup> with the increase of iron loading from 5 to 40% (Fig. 5b). This confirms that nanoFe<sup>0</sup> is responsible for the uptake of Cu<sup>2+</sup>. However, Q<sub>Fe-Cu</sub> and the Fe use ratio values showed a decrease as the iron loading rose. In particular, the Fe use ratio decreased from 58 to 9% as iron loading went up from 5 to 40%. To investigate this, we characterized BC-G@Fe<sup>0</sup> samples by SEM. NanoFe<sup>0</sup> particles were well-dispersed on the BC surfaces at a 5%

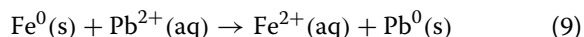
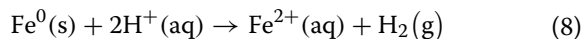
iron loading (Fig. 5c). At a 10% loading, nanoFe<sup>0</sup> clusters appeared because particle aggregation occurred. This aggregation became increasingly severe at higher loading (Fig. 5d–f), causing the Fe use ratio to drop at higher iron loadings.

### 3.3 Heavy metal removal study

BC-G@Fe<sup>0</sup> samples produced from FeCl<sub>2</sub>-impregnated-BC carbonization (route II) with 15% iron loading at 1000 °C were used for the heavy metal ion removal study. The uptake of Pb<sup>2+</sup> by BC-G@Fe<sup>0</sup> was pH-dependent. The effect of solution pH was determined within the pH range of 1–7 (Fig. 6a). The uptake capacity of Pb<sup>2+</sup> drastically increased from 0.006 to 0.17 mmol g<sup>-1</sup> as the solution pH increased from 1 to 3, while the capacity only slightly changed as the pH increased from 3 to 7. The removal of Pb<sup>2+</sup> is minimized at low solution pH (i.e., pH 1 and 2) by



the reaction between Fe<sup>0</sup> and H<sup>+</sup> resulting in oxidation of Fe<sup>0</sup> to Fe<sup>2+</sup> (Eq. 8). At pH 3–7, the Pb<sup>2+</sup> removal is mainly attributed to the reduction of Pb<sup>2+</sup> to Pb<sup>0</sup> by Fe<sup>0</sup> (Eq. 9).



XPS confirmed the presence of Pb<sup>0</sup> on the surface of BC-G@Fe<sup>0</sup> after Pb<sup>2+</sup> uptake (Fig. 6j). Additionally, the presence of Pb<sup>2+</sup> on the surface of BC-G@Fe<sup>0</sup> can be attributed to either the oxidation of reduced Pb<sup>0</sup> nanoparticles or precipitation of Pb<sup>2+</sup> compounds during Fe<sup>0</sup> dissolution (Zhang et al. 2021b).

Kinetic and isotherm studies were carried out at the initial pH of 6. The Pb<sup>2+</sup> removal rapidly increased in the first 15 min and reached equilibrium (Fig. 6b). The data were fitted to both pseudo-first-order (1st-order) and pseudo-second-order (2nd-order) models with R<sup>2</sup> values of 0.966 and 0.918 (Additional file 1: Table S2), respectively. The Langmuir (R<sup>2</sup>=0.711) and Freundlich (R<sup>2</sup>=0.929) models fitted to isotherm data favoring a multilayer model (Fig. 6c). The maximum Langmuir adsorption capacity was calculated to be 0.31 mmol g<sup>-1</sup>.

The uptake of Cu<sup>2+</sup> into BC-G@Fe<sup>0</sup> is highly pH dependent like Pb<sup>2+</sup>. The effect of solution pH was

determined from pH 1–6 (Fig. 6d). The uptake capacity of Cu<sup>2+</sup> dramatically increased from 0 to 1.04 mmol g<sup>-1</sup> as the solution pH increased from 1 to 3. The uptake capacity slightly differs as the pH increases from 3 to 6. Like Pb<sup>2+</sup>, Cu<sup>2+</sup> removal is low at acidic pH (i.e., pH 1 and 2) by Eq. 1. At pH 3–7, the Cu<sup>2+</sup> removal is mainly attributed to the reduction of Cu<sup>2+</sup> to Cu<sup>0</sup> by Fe<sup>0</sup> (Eq. 7). XPS of BC-G@Fe<sup>0</sup> after Cu<sup>2+</sup> uptake confirms the reduction of Cu<sup>2+</sup> to Cu<sup>0</sup> (Fig. 6k). Moreover, Cu<sup>2+</sup> is also observed on the surface of BC-G@Fe<sup>0</sup>, which can be attributed to the oxidation of reduced Cu<sup>0</sup> and the precipitated Cu<sup>2+</sup> compounds during Fe<sup>0</sup> dissolving.

Kinetic and isotherm studies were carried out at the initial pH of 5. The Cu<sup>2+</sup> uptake rapidly increased in the first 10 min, then slowly increased between 10 and 20 min, and finally reached equilibrium after 20 min. Over 90% of ultimate Cu<sup>2+</sup> uptake was achieved within 5 min, showing the high removal kinetics of our BC-G@Fe<sup>0</sup> toward Cu<sup>2+</sup>. The data were fitted to both pseudo-first-order and pseudo-second-order models with R<sup>2</sup> values of 0.803 and 0.754, respectively (Fig. 6e). Figure 6f shows concentration-dependent Cu<sup>2+</sup> removal by BC-G@Fe<sup>0</sup>. Adsorption isotherms were drawn to illustrate the relationship between Cu<sup>2+</sup> concentration at the equilibrium and the adsorbed Cu<sup>2+</sup> concentration. The Langmuir (R<sup>2</sup>=0.984) and Freundlich (R<sup>2</sup>=0.904) models gave good fits to isotherm data (Additional file 1:

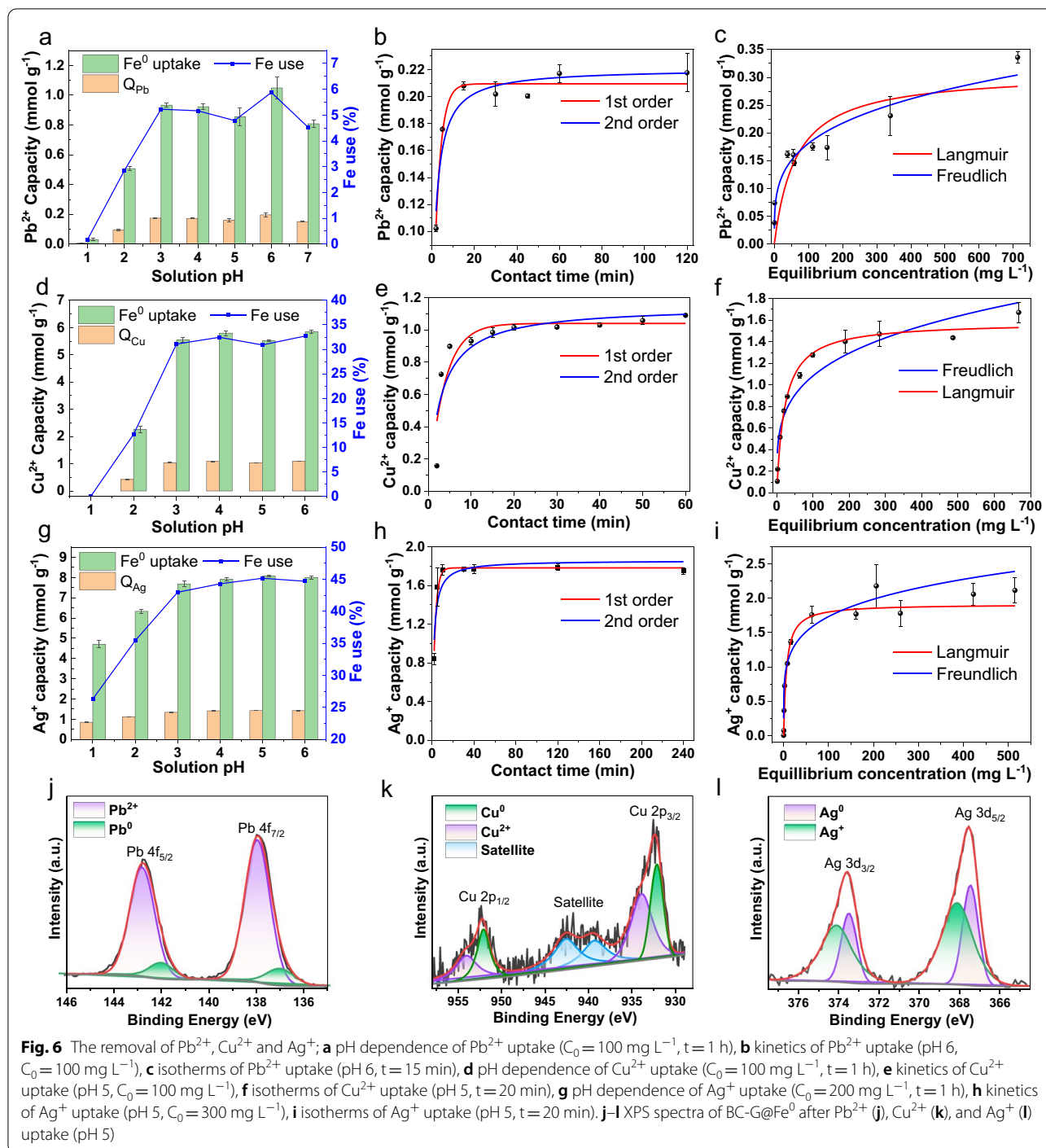
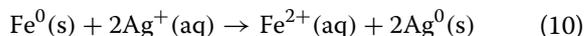


Table S2). The maximum Langmuir adsorption capacity is calculated to be 1.58 mmol g<sup>-1</sup>.

The uptake of Ag<sup>+</sup> by BC-G@Fe<sup>0</sup> is also pH-dependent. The effect of solution pH is determined within the pH range of 1–6 (Fig. 6g). The uptake capacity of Ag<sup>+</sup> increased from 0.851 to 1.345 mmol g<sup>-1</sup> as the solution pH increased from 1 to 3. The uptake capacity

becomes almost a constant value as the pH increases from 3 to 6. Like Cu<sup>2+</sup> and Pb<sup>2+</sup>, Ag<sup>+</sup> removal is low at acidic pH (i.e., pH 1 and 2) by Eq. 1. At pH 3–6, the Ag<sup>+</sup> removal is mainly attributed to one electron reductions of two Ag<sup>+</sup> to Ag<sup>0</sup> by Fe<sup>0</sup> (Eq. 10).



**Table 1** Uptake capacity of different nanoscale zero-valent iron (nanoFe<sup>0</sup>) adsorbents towards Pb<sup>2+</sup>, Cu<sup>2+</sup> and Ag<sup>+</sup> in aqueous solutions

Metal ion	Adsorbent	Method	Size of nanoFe <sup>0</sup>	Sorption conditions	Fe content (%)	Uptake Capacity (mmol g <sup>-1</sup> )	Iron uptake Capacity (mmol g <sup>-1</sup> )	References
Pb <sup>2+</sup>	Reed biochar supported nanoFe <sup>0</sup>	NaBH <sub>4</sub> reduction	10.77–13.34 nm	Oxic 30 °C, pH 6.0 ± 0.2	67	0.18	0.27	Zhu et al. (2017)
	Hydrophilic biochar-nanoFe <sup>0</sup> from corn stalk	Acid ammonium persulfate oxidation	100–230 nm	Oxic 25 ± 1 °C, pH 6.0	50	2.85	5.70	Li et al. (2020)
	Lignin-based few-layered graphene-encapsulated iron nanoparticles	Carbothermal reduction	5–15 nm	Oxic 25 °C, pH 6.0	14	0.62	4.43	Zhang et al. (2021b)
	Shell biomass material supported nanoFe <sup>0</sup>	NaBH <sub>4</sub> reduction	60 nm	Oxic 30 °C, pH 6.0	21	0.45	2.14	Wang et al. (2020)
	Exhausted coffee ground supported nanoFe <sup>0</sup>	NaBH <sub>4</sub> reduction	< 100 nm	Oxic 25 °C, pH 6.0	17	0.79	4.65	Park et al. (2019)
	NanoFe <sup>0</sup> -magnetic biochar composites	Reduction by honey	NA	Oxic 30 °C, pH 6.0	10	0.29	2.90	Rama Chandraiah (2016)
	Chitosan and biochar synergistically modified sulfurized nanoFe <sup>0</sup>	NaBH <sub>4</sub> reduction	NA	Oxic 25 °C	NA	1.38	NA	Xu et al. (2022)
	<b>BC-G@Fe<sup>0</sup></b>	<b>Carbothermal reduction</b>	<b>20–100 nm</b>	<b>Oxic 25 °C, pH 6.0</b>	<b>18</b>	<b>0.31</b>	<b>1.72</b>	<b>This study</b>
Cu <sup>2+</sup>	Amino-modified biochar supporting nanoFe <sup>0</sup>	NA	~50 nm	Oxic 25 °C, pH 5.0–6.0	50	0.12	0.24	Yang et al. (2018)
	Rubber seed shell supported nanoFe <sup>0</sup>	NaBH <sub>4</sub> reduction	NA	Oxic 30 °C, pH 6.0	50	0.76	1.52	Prabu et al. (2017)
	Reed biochar supported nanoFe <sup>0</sup>	NaBH <sub>4</sub> reduction	10.77–13.34 nm	Oxic 30 °C, pH 6.0 ± 0.2	67	0.48	0.72	Zhu et al. (2017)
	Goethite@bagasse biochar	Carbothermal reduction	NA	Oxic 25 °C, pH 6.0	25	0.74	2.96	Cai et al. (2021)
	Goethite@straw biochar	Carbothermal reduction	NA	Oxic 25 °C, pH 6.0	25	0.66	2.64	Cai et al. (2021)
	Kenaf bar biochar supported nanoFe <sup>0</sup>	NaBH <sub>4</sub> reduction	100 nm	Oxic pH 6.0	41	1.01	2.46	Liu et al. (2018)
	Biochar (≤ 50 mesh) supported nanoFe <sup>0</sup>	NaBH <sub>4</sub> reduction	NA	Oxic 25 °C	17	4.11	24.18	Hasan et al. (2020)
	<b>BC-G@Fe<sup>0</sup></b>	<b>Carbothermal reduction</b>	<b>20–100 nm</b>	<b>Oxic 25 °C, pH 5.0</b>	<b>18</b>	<b>1.58</b>	<b>8.78</b>	<b>This study</b>

**Table 1** (continued)

Metal ion	Adsorbent	Method	Size of nanoFe <sup>0</sup>	Sorption conditions	Fe content (%)	Uptake Capacity (mmol g <sup>-1</sup> )	Iron uptake Capacity (mmol g <sup>-1</sup> )	References
Ag <sup>+</sup>	Bamboo derived biochar supported nanoFe <sup>0</sup>	NaBH <sub>4</sub> reduction	26–40 nm	Oxic 22 ± 0.5 °C	NA	1.26	NA	Wang et al. (2017b)
	Fe <sup>0</sup> -biochar composite with chitosan (BBCF)	Dispersing and soldering commercial nanoFe <sup>0</sup> using chitosan	28 nm	Oxic 22 ± 0.5 °C	33	6.07	18.39	Zhou et al. (2014)
	Bamboo derived HNO <sub>3</sub> acid modified nanoFe <sup>0</sup>	NaBH <sub>4</sub> reduction	30.5 nm	Oxic 22 ± 0.5 °C	10	1.85	18.5	Wang et al. (2017a)
	<b>BC-G@Fe<sup>0</sup></b>	<b>Carbothermal reduction</b>	<b>20–100 nm</b>	<b>Oxic 25 °C, pH 5.0</b>	<b>18</b>	<b>1.91</b>	<b>10.61</b>	<b>This study</b>

Bold represent the sample prepared from this study

The reduction of Ag<sup>+</sup> to Ag<sup>0</sup> was confirmed by XPS of BC-G@Fe<sup>0</sup> after Ag<sup>+</sup> uptake (Fig. 6l). Moreover, the presence of Ag<sup>+</sup> on the surface of BC-G@Fe<sup>0</sup> can be attributed to the oxidation of reduced Ag<sup>0</sup> and the precipitated Ag<sup>+</sup> compounds during Fe<sup>0</sup> dissolving.

Kinetic and isotherm studies were carried out at the initial pH of 5 (Fig. 6h, i). The Ag<sup>+</sup> removal increased in the first 10 min and reached equilibrium after 20 min. The data were fitted to both pseudo-first-order and pseudo-second-order models with R<sup>2</sup> values of 0.971 and 0.824 (Additional file 1: Table S2), respectively. The Langmuir (R<sup>2</sup> = 0.99) and Freundlich (R<sup>2</sup> = 0.74) models fitted to isotherm data favoring a monolayer model. The maximum Langmuir adsorption capacity was calculated to be 1.913 mmol g<sup>-1</sup>.

BC-G@Fe<sup>0</sup> shows the highest uptake capacity for Ag<sup>+</sup>, followed by Cu<sup>2+</sup> and then Pb<sup>2+</sup>. This is expected because their reduction potentials are in the following order from high to low Ag<sup>+</sup> (0.80 V) > Cu<sup>2+</sup> (0.34 V) > Pb<sup>2+</sup> (-0.13 V). In particular, the Langmuir capacity of Pb<sup>2+</sup> is four and five times lower than that of Cu<sup>2+</sup> and Pb<sup>2+</sup>, respectively. Such low capacity is because its reduction potential is lower than H<sup>+</sup> (0.00 V), as a result, nanoFe<sup>0</sup> in BC-G@Fe<sup>0</sup> is mainly consumed by H<sup>+</sup> during Pb<sup>2+</sup> removal (reaction 8) (Busch et al. 2021). From stoichiometry calculations, one mole of nanoFe<sup>0</sup> could uptake two moles of Ag<sup>+</sup> and one mole Cu<sup>2+</sup> via single-displacement reactions, respectively. However, the Langmuir capacity of Ag<sup>+</sup> is only 20% higher than that of Cu<sup>2+</sup>, which is much lower than expected. Heavy metal removal by BC-G@Fe<sup>0</sup> is a mass transfer process, where the metal ions migrate to the nanoFe<sup>0</sup> surface and are followed by

surface reduction and deposition. Despite BC-G@Fe<sup>0</sup> showing a higher potential for Ag<sup>+</sup> uptake than Cu<sup>2+</sup> stoichiometrically, the exposed nanoFe<sup>0</sup> surface area is limited. Once the exposed surfaces are occupied by the reduced heavy metal nanoparticles, the uptake is terminated. Hence, the overall Ag<sup>+</sup> capacity is much less than the expected value.

Table 1 displays Pb<sup>2+</sup>, Cu<sup>2+</sup> and Ag<sup>+</sup> removal in aqueous solutions using different nanoFe<sup>0</sup> adsorbents. Our BC-G@Fe<sup>0</sup> shows higher uptake capacities for Pb<sup>2+</sup>, Cu<sup>2+</sup> and Ag<sup>+</sup> compared to some of the reported nanoFe<sup>0</sup> adsorbents. For instance, nanoFe<sup>0</sup> supported by reed biochar has a Pb<sup>2+</sup> uptake capacity of 0.18 mmol g<sup>-1</sup> (Zhu et al. 2017), which is lower than that of the present study. Additionally, BC-G@Fe<sup>0</sup> exhibits a 13 times greater Cu<sup>2+</sup> uptake capacity than that of amino-modified biochar supporting nanoFe<sup>0</sup> (Yang et al. 2018). Furthermore, our BC-G@Fe<sup>0</sup> exhibits a higher Ag<sup>+</sup> uptake capacity of 1.91 mmol g<sup>-1</sup> in comparison to bamboo char supported nanoFe<sup>0</sup> using the NaBH<sub>4</sub> method (Wang et al. 2017b). Li et al. (2020) produced hydrophilic biochar-nanoFe<sup>0</sup>, which had a higher Pb<sup>2+</sup> uptake capacity than that of our BC-G@Fe<sup>0</sup>. (Li et al. 2020). This can be attributed to their hydrophilic biochar having a high adsorption capacity to Pb<sup>2+</sup> because of its abundant functional groups. Similarly, expensive chitosan-stabilized nanoFe<sup>0</sup> particles prepared by Chen et al. also exhibited a higher capacity for than this study (Chen et al. 2019) because chitosan has a high Pb<sup>2+</sup> sorption capacity via complexation (Fan et al. 2020a). However, they have followed the NaBH<sub>4</sub> reduction method which involves hazardous chemicals

(Chen et al. 2019). Hasan et al. revealed approximately three times higher capacity for  $\text{Cu}^{2+}$  than this study (Hasan et al. 2020). However, they employed  $\text{NaBH}_4$  reduction which is not sustainable for scale up removal of water contaminants. Zhou et al. showed three times higher sorption capacity for  $\text{Ag}^+$  than this study. They have also used chitosan which has an additional advantage of adsorbing  $\text{Ag}^+$  through chitosan amino group complexation, hence, uplifting the uptake of heavy metal ions (Zhou et al. 2014).

#### 4 Conclusion

This study explored BC-G@Fe<sup>0</sup> composite synthesis by two carbothermal reduction routes and their application to remove heavy metal ions. Route I employed direct carbothermal reduction of iron salt-impregnated biomass, which generated BC-G@Fe<sup>0</sup>-containing graphene-encapsulated Fe<sub>3</sub>C nanoparticles. This route led to low heavy metal removal efficiency (i.e., <0.3 mmol g<sup>-1</sup> for Cu<sup>2+</sup>). Route II first pre-pyrolyzed biomass at 600 °C to biochar and then impregnated that biochar with iron salt. This was followed by carbothermal reduction. Carbonaceous gases (e.g., CH<sub>4</sub> and CO) were responsible for Fe<sub>3</sub>C formation. Because they were removed during biomass pyrolysis, subsequent carbothermal reduction of iron salt-impregnated biochar gave BC-G@Fe<sup>0</sup> containing graphene-encapsulated nanoFe<sup>0</sup>. This results in high heavy metal removal efficiency (i.e., 1.58 mmol g<sup>-1</sup> for Cu). At our optimized conditions, i.e., the pre-pyrolyzing step employing FeCl<sub>2</sub> as the iron resource, 15% iron loading, 1000 °C carbonization for 1 h, the produced BC-G@Fe<sup>0</sup> had Pb<sup>2+</sup>, Cu<sup>2+</sup>, and Ag<sup>+</sup> removal capacities of 0.30, 1.58, and 1.91 mmol g<sup>-1</sup>, respectively. Future studies will focus on using BC-G@Fe<sup>0</sup> to remove heavy metals from soil.

#### Supplementary Information

The online version contains supplementary material available at <https://doi.org/10.1007/s42773-022-00196-5>.

**Additional file 1: Figure S1.** Gas adsorption study of iron salts-derived BC-G@Fe<sup>0</sup> (a) N<sub>2</sub> adsorption isotherms of iron salts-derived BC-G@Fe<sup>0</sup>. (b) Specific surface area and pore volume results. **Figure S2.** Gas adsorption study of BC-G@Fe<sup>0</sup>-X (a) N<sub>2</sub> adsorption isotherms of BC-G@Fe<sup>0</sup>-600-BC-G@Fe<sup>0</sup>-1000 (b) Specific surface area and pore volume results. **Figure S3.** Spot diameter distribution of the Fe<sup>0</sup> nanoparticles made with different impregnated iron salts (route II) shown in the SEM images (Fig. 3h–k). **Figure S4.** SEM image and EDS elemental mapping of BC-G@Fe<sup>0</sup>-600. **Figure S5.** SEM image and EDS elemental mapping of BC-G@Fe<sup>0</sup>-700. **Figure S6.** SEM image and EDS elemental mapping of BC-G@Fe<sup>0</sup>-900. **Figure S7.** SEM image and EDS elemental mapping of BC-G@Fe<sup>0</sup>-1000. **Table S1.** Fe content in all BC-G@Fe<sup>0</sup> products prepared by route II. **Table S2.** Kinetic and Isotherm Parameters for Pb<sup>2+</sup>, Cu<sup>2+</sup> and Ag<sup>+</sup> Adsorptions onto BC-G@Fe<sup>0</sup>

#### Acknowledgements

The authors thank USDA-NIFA provide the funding support for this project. The authors also the Institute of Imaging and Analytical Technology, Mississippi State University (MSU) for providing access to XRD, SEM, and TEM characterizations. This manuscript is publication #SB1077 of the Department of Sustainable Bioproducts, MSU. This publication is a contribution of the Forest and Wildlife Research Center, MSU.

#### Author contributions

TNK: Investigation, Methodology, Data analysis, Writing original draft, Review & editing. RMON: Investigation, Methodology, Data analysis. CMN: Investigation, Methodology. PMR: Methodology, Data analysis. RVKGT: Methodology. CUPJR: Scientific discussion, Review & editing. YK: Funding acquisition, Scientific discussion. TM: Funding acquisition, Methodology, Scientific discussion; JZ: Funding acquisition, Scientific discussion, Review & editing. XZ: Funding acquisition, Project administration, Conceptualization, Investigation, Data analysis, Writing original draft, Review & editing. All authors read and approved the final manuscript.

#### Funding

This work was supported by the USDA National Institute of Food and Agriculture (NIFA) (Grant No. 2020-65210-30763).

#### Availability of data and materials

The authors declare that data will be made available on reasonable request.

#### Declarations

#### Competing interests

The authors declare no competing financial interests.

#### Author details

<sup>1</sup>Department of Sustainable Bioproducts, Mississippi State University, Mississippi State, MS 39762, USA. <sup>2</sup>Department of Chemistry, Mississippi State University, Mississippi State, MS 39762, USA. <sup>3</sup>Institute for Imaging & Analytical Technologies, Mississippi State University, Mississippi State, MS 39762, USA.

Received: 22 August 2022 Revised: 1 December 2022 Accepted: 12 December 2022

Published online: 28 December 2022

#### References

- Asif I, Baig N, Sher M, Ul-Hamid A, Altaf M, Mumtaz A, Sohail M (2021) MOF derived novel zero-valent iron@graphitic carbon-based nanoreactors for selective reduction of hazardous 4-nitrophenol. *Clean Eng Technol* 2:100081. <https://doi.org/10.1016/j.clet.2021.100081>
- Bagheri M, Jafari SM, Eikani MH (2021) Ultrasonic-assisted production of zero-valent iron-decorated graphene oxide/activated carbon nanocomposites: chemical transformation and structural evolution. *Mater Sci Eng C* 118:111362. <https://doi.org/10.1016/j.msec.2020.111362>
- Briffa J, Sinagra E, Blundell R (2020) Heavy metal pollution in the environment and their toxicological effects on humans. *Heliyon* 6:e04691. <https://doi.org/10.1016/j.heliyon.2020.e04691>
- Busch M, Ahlberg E, Laasonen K (2021) From absolute potentials to a generalized computational standard hydrogen electrode for aqueous and non-aqueous solvents. *Phys Chem Chem Phys* 23:11727–11737. <https://doi.org/10.1039/D1CP00499A>
- Cai M, Zeng J, Chen Y, He P, Chen F, Wang X, Liang J, Gu C, Huang D, Zhang K, Gan M, Zhu J (2021) An efficient, economical, and easy mass production biochar supported zero-valent iron composite derived from direct-reduction natural goethite for Cu(II) and Cr(VI) remove. *Chemosphere* 285:131539. <https://doi.org/10.1016/j.chemosphere.2021.131539>
- Chen X-L, Li F, Xie XJ, Li Z, Chen L (2019) Nanoscale zero-valent iron and chitosan functionalized *Eichhornia crassipes* biochar for efficient hexavalent chromium removal. *Int J Environ Res Public Health* 16:3046. <https://doi.org/10.3390/ijerph16173046>

- Chen C, Liu J, Gen C, Liu Q, Zhu X, Qi W, Wang F (2021) Synthesis of zero-valent iron/biochar by carbothermal reduction from wood waste and iron mud for removing rhodamine B. *Environ Sci Pollut Res* 28:48556–48568. <https://doi.org/10.1007/s11356-021-13962-y>
- Crane RA, Scott TB (2012) Nanoscale zero-valent iron: future prospects for an emerging water treatment technology. *J Hazard Mater* 211–212:112–125. <https://doi.org/10.1016/j.jhazmat.2011.11.073>
- Ezzatahmedi N, Ayoko GA, Millar GJ, Speight R, Yan C, Li J, Li S, Zhu J, Xi Y (2017) Clay-supported nanoscale zero-valent iron composite materials for the remediation of contaminated aqueous solutions: a review. *Chem Eng J* 312:336–350. <https://doi.org/10.1016/j.cej.2016.11.154>
- Fan H, Ren H, Ma X, Zhou S, Huang J, Jiao W, Qi G, Liu Y (2020a) High-gravity continuous preparation of chitosan-stabilized nanoscale zero-valent iron towards Cr(VI) removal. *Chem Eng J* 390:124639. <https://doi.org/10.1016/j.cej.2020.124639>
- Fan J, Chen X, Xu Z, Xu X, Zhao L, Qiu H, Cao X (2020b) One-pot synthesis of nZVI-embedded biochar for remediation of two mining arsenic-contaminated soils: arsenic immobilization associated with iron transformation. *J Hazard Mater* 398:122901. <https://doi.org/10.1016/j.jhazmat.2020.122901>
- Farzi N, Hydarifard M-H, Izadi ME, Sabzyan H (2020) Investigation of iron carbide ( $\text{Fe}_3\text{C}$ ) corrosion in water and acidic solution using ReaxFF molecular dynamics. *J Mol Liq* 318:114006. <https://doi.org/10.1016/j.molliq.2020.114006>
- Florea AF, Lu C, Hansen HCB (2022) A zero-valent iron and zeolite filter for nitrate recycling from agricultural drainage water. *Chemosphere* 287:131993. <https://doi.org/10.1016/j.chemosphere.2021.131993>
- Eisler R (1996) Silver hazards to fish, wildlife, and invertebrates: a synoptic review. Contaminant Hazard Reviews Report 32; Biological Report 32 U.S. National Biological Service. <https://pubs.er.usgs.gov/publication/5200169>
- Hasan MS, Geza M, Vasquez R, Chilkoor G, Gadhamshetty V (2020) Enhanced heavy metal removal from synthetic stormwater using nanoscale zero-valent iron-modified biochar. *Water Air Soil Pollut* 231:220. <https://doi.org/10.1007/s11270-020-04588-w>
- Huang X, Zhang F, Peng K, Liu J, Lu L, Li S (2020) Effect and mechanism of graphene structured palladized zero-valent iron nanocomposite (nZVI-Pd/NG) for water denitration. *Sci Rep* 10:9931. <https://doi.org/10.1038/s41598-020-66725-z>
- Hunter RD, Ramírez-Rico J, Schnepf Z (2022) Iron-catalyzed graphitization for the synthesis of nanostructured graphitic carbons. *J Mater Chem A*. <https://doi.org/10.1039/D1TA09654K>
- Jiang S-F, Ling L-L, Chen W-J, Liu W-J, Li D-C, Jiang H (2019) High efficient removal of bisphenol A in a peroxymonosulfate/iron functionalized biochar system: mechanistic elucidation and quantification of the contributors. *Chem Eng J* 359:572–583. <https://doi.org/10.1016/j.cej.2018.11.124>
- Jiang Q, Zhang Y, Jiang S, Wang Y, Li H, Han W, Qu J, Wang L, Hu Y (2021) Graphene-like carbon sheet-supported nZVI for efficient atrazine oxidation degradation by persulfate activation. *Chem Eng J* 403:126309. <https://doi.org/10.1016/j.cej.2020.126309>
- Jiao W, Song Y, Zhang D, Chang G, Fan H, Liu Y (2019) Nanoscale zero-valent iron modified with carboxymethyl cellulose in an impinging stream-rotating packed bed for the removal of lead(II). *Adv Powder Technol* 30:2251–2261. <https://doi.org/10.1016/j.japt.2019.07.005>
- Lan Y, Chen J, Zhang H, Zhang W, Yang J (2020) Fe/Fe<sub>3</sub>C nanoparticle-decorated N-doped carbon nanofibers for improving the nitrogen selectivity of electrocatalytic nitrate reduction. *J Mater Chem A*. <https://doi.org/10.1039/D0TA02317E>
- Li Z, Wang L, Meng J, Liu X, Xu J, Wang F, Brookes P (2018) Zeolite-supported nanoscale zero-valent iron: new findings on simultaneous adsorption of Cd(II), Pb(II), and As(III) in aqueous solution and soil. *J Hazard Mater* 344:1–11. <https://doi.org/10.1016/j.jhazmat.2017.09.036>
- Li S, Yang F, Li J, Cheng K (2020) Porous biochar-nanoscale zero-valent iron composites: synthesis, characterization and application for lead ion removal. *Sci Total Environ* 746:141037. <https://doi.org/10.1016/j.scitotenv.2020.141037>
- Liu X-W, Huo C-F, Li Y-W, Wang J, Jiao H (2012) Energetics of carbon deposition on Fe(100) and Fe(110) surfaces and subsurfaces. *Surf Sci* 606:733–739. <https://doi.org/10.1016/j.susc.2011.12.018>
- Liu J, Yu B, Zhang Q, Hou L, Huang Q, Song C, Wang S, Wu Y, He Y, Zou J, Huang H (2015) Synthesis and magnetic properties of Fe<sub>3</sub>C–C core–shell nanoparticles. *Nanotechnology* 26:085601. <https://doi.org/10.1088/0957-4484/26/8/085601>
- Liu C-M, Diao Z-H, Huo W-Y, Kong L-J, Du J-J (2018) Simultaneous removal of Cu<sup>2+</sup> and bisphenol A by a novel biochar-supported zero valent iron from aqueous solution: synthesis, reactivity and mechanism. *Environ Pollut* 239:698–705. <https://doi.org/10.1016/j.envpol.2018.04.084>
- Liu T, Zhang Z, Wang Z, Wang Z-L, Bush R (2019) Highly efficient and rapid removal of arsenic(III) from aqueous solutions by nanoscale zero-valent iron supported on a zirconium 1,4-dicarboxybenzene metal–organic framework (UiO-66 MOF). *RSC Adv* 9:39475–39487. <https://doi.org/10.1039/C9RA08595E>
- Liu X, Yang L, Zhao H, Wang W (2020) Pyrolytic production of zerovalent iron nanoparticles supported on rice husk-derived biochar: simple, in situ synthesis and use for remediation of Cr(VI)-polluted soils. *Sci Total Environ* 708:134479. <https://doi.org/10.1016/j.scitotenv.2019.134479>
- Ma D, Yang Y, Liu B, Xie G, Chen C, Ren N, Xing D (2021) Zero-valent iron and biochar composite with high specific surface area via K<sub>2</sub>FeO<sub>4</sub> fabrication enhances sulfadiazine removal by persulfate activation. *Chem Eng J* 408:127992. <https://doi.org/10.1016/j.cej.2020.127992>
- Madduri S, Elsayed I, Hassan EB (2020) Novel oxone treated hydrochar for the removal of Pb(II) and methylene blue (MB) dye from aqueous solutions. *Chemosphere* 260:127683. <https://doi.org/10.1016/j.chemosphere.2020.127683>
- Mun SP, Cai Z, Zhang J (2015) Preparation of Fe-cored carbon nanomaterials from mountain pine beetle-killed pine wood. *Mater Lett* 142:45–48. <https://doi.org/10.1016/j.matlet.2014.11.053>
- Neeli ST, Ramsurn H (2018) Synthesis and formation mechanism of iron nanoparticles in graphitized carbon matrices using biochar from biomass model compounds as a support. *Carbon* 134:480–490. <https://doi.org/10.1016/j.carbon.2018.03.079>
- Ng WM, Lim JK (2022) Complex interplay between colloidal stability, transport, chemical reactivity and magnetic separability of polyelectrolyte-functionalized nanoscale zero-valent iron particles (nZVI) toward their environmental engineering application. *Colloid Interface Sci Commun* 46:100582. <https://doi.org/10.1016/j.colcom.2021.100582>
- Park MH, Jeong S, Lee G, Park H, Kim JY (2019) Removal of aqueous-phase Pb(II), Cd(II), As(III), and As(V) by nanoscale zero-valent iron supported on exhausted coffee grounds. *Waste Manag* 92:49–58. <https://doi.org/10.1016/j.wasman.2019.05.017>
- Prabu D, Parthiban R, Ponnusamy SK, Anbalagan S, John R, Titus T (2017) Sorption of Cu(II) ions by nano-scale zero valent iron supported on rubber seed shell. *IET Nanobiotechnol* 11:714–724. <https://doi.org/10.1049/iet-nbt.2016.0224>
- Rama Chandiraiah M (2016) Facile synthesis of zero valent iron magnetic biochar composites for Pb(II) removal from the aqueous medium. *Alex Eng J* 55:619–625. <https://doi.org/10.1016/j.aej.2015.12.015>
- Samaraweera H, Nawalage S, Nayanathara RMO, Peiris C, Karunaratne TN, Gunatilake SR, Thirumalai RVKG, Zhang J, Zhang X, Mlnsa T (2022) In situ synthesis of zero-valent iron-decorated lignite carbon for aqueous heavy metal remediation. *Processes* 10:1659. <https://doi.org/10.3390/pr10081659>
- Tchounwou PB, Yedjou CG, Patlolla AK, Sutton DJ (2012) Heavy metal toxicity and the environment. In: Luch A (ed) *Molecular, clinical and environmental toxicology, experientia supplementum*. Springer, Basel, pp 133–164. [https://doi.org/10.1007/978-3-7643-8340-4\\_6](https://doi.org/10.1007/978-3-7643-8340-4_6)
- Thommes M, Kaneko K, Neimark AV, Olivier JP, Rodriguez-Reinoso F, Rouquerol J, Sing KSW (2015) Physisorption of gases, with special reference to the evaluation of surface area and pore size distribution (IUPAC technical report). *Pure Appl Chem* 87:1051–1069. <https://doi.org/10.1515/pac-2014-1117>
- Thompson E, Danks AE, Bourgeois L, Schnepf Z (2015) Iron-catalyzed graphitization of biomass. *Green Chem* 17:551–556. <https://doi.org/10.1039/C4GC01673D>
- Vinogradov NA, Simonov KA, Generalov AV, Drnec J, Carli F, Vinogradov AS, Preobrajenski AB, Mårtensson N, Felici R (2017) The structural evolution of graphene/Fe(110) systems upon annealing. *Carbon* 111:113–120. <https://doi.org/10.1016/j.carbon.2016.09.058>
- Wang S, Zhou Y, Gao B, Wang X, Yin X, Feng K, Wang J (2017a) The sorptive and reductive capacities of biochar supported nanoscale zero-valent

- iron (nZVI) in relation to its crystallite size. *Chemosphere* 186:495–500. <https://doi.org/10.1016/j.chemosphere.2017.08.014>
- Wang S, Zhao M, Zhao Y, Wang N, Bai J, Feng K, Zhou Y, Chen W, Wen F, Wang S, Wang X, Wang J (2017b) Pyrogenic temperature affects the particle size of biochar-supported nanoscale zero valent iron (nZVI) and its silver removal capacity. *Chem Speciat Bioavailab* 29:179–185. <https://doi.org/10.1080/09542299.2017.1395712>
- Wang S, Zhao M, Zhou M, Li YC, Wang J, Gao B, Sato S, Feng K, Yin W, Igalavithana AD, Oleszczuk P, Wang X, Ok YS (2019) Biochar-supported nZVI (nZVI/BC) for contaminant removal from soil and water: a critical review. *J Hazard Mater* 373:820–834. <https://doi.org/10.1016/j.jhazmat.2019.03.080>
- Wang Z, Wu X, Luo S, Wang Y, Tong Z, Deng Q (2020) Shell biomass material supported nano-zero valent iron to remove  $Pb^{2+}$  and  $Cd^{2+}$  in water. *R Soc Open Sci* 7:201192. <https://doi.org/10.1098/rsos.201192>
- Wani AL, Ara A, Usmani JA (2015) Lead toxicity: a review. *Interdiscip Toxicol* 8:55–64. <https://doi.org/10.1515/intox-2015-0009>
- Wirth CT, Bayer BC, Gamalski AD, Esconjauregui S, Weatherup RS, Ducati C, Baehtz C, Robertson J, Hofmann S (2012) The phase of iron catalyst nanoparticles during carbon nanotube growth. *Chem Mater* 24:4633–4640. <https://doi.org/10.1021/cm301402g>
- Xing R, He J, Hao P, Zhou W (2020) Graphene oxide-supported nanoscale zero-valent iron composites for the removal of atrazine from aqueous solution. *Colloids Surf Physicochem Eng Asp* 589:124466. <https://doi.org/10.1016/j.colsurfa.2020.124466>
- Xu H, Li X, Gao M, Hu X, Zhang X, Li Y, Xu X, Hu J, Tang C, Hu Xi (2022) Chitosan and biochar synergize the efficient elimination of lead from wastewater by sulfidised nano-zero-valent iron. *J Environ Chem Eng* 10:107101. <https://doi.org/10.1016/j.jece.2021.107101>
- Yan Q, Wan C, Liu J, Gao J, Yu F, Zhang J, Cai Z (2013) Iron nanoparticles in situ encapsulated in biochar-based carbon as an effective catalyst for the conversion of biomass-derived syngas to liquid hydrocarbons. *Green Chem* 15:1631–1640. <https://doi.org/10.1039/C3GC37107G>
- Yan Q, Li J, Zhang X, Zhang J, Cai Z (2018a) Synthetic bio-graphene based nanomaterials through different iron catalysts. *Nanomaterials* 8:840. <https://doi.org/10.3390/nano8100840>
- Yan Q, Li J, Zhang X, Zhang J, Cai Z (2018b) In situ formation of graphene-encapsulated iron nanoparticles in carbon frames through catalytic graphitization of kraft lignin. *Nanomater Nanotechnol* 8:1–12. <https://doi.org/10.1177/1847980418818955>
- Yan Q, Zhang X, Li J, Hassan EB, Wang C, Zhang J, Cai Z (2018c) Catalytic conversion of kraft lignin to bio-multilayer graphene materials under different atmospheres. *J Mater Sci* 53:8020–8029. <https://doi.org/10.1007/s10853-018-2172-0>
- Yan Q, Li J, Zhang X, Zhang J, Cai Z (2019) Mass production of graphene materials from solid carbon sources using a molecular cracking and welding method. *J Mater Chem A* 7:13978–13985. <https://doi.org/10.1039/C9TA01332F>
- Yang J, Ma T, Li X, Tu J, Dang Z, Yang C (2018) Removal of heavy metals and metalloids by amino-modified biochar supporting nanoscale zero-valent iron. *J Environ Qual* 47:1196–1204. <https://doi.org/10.2134/jeq2017.08.0320>
- Yang K, Xu J, Zhang M, Lin D (2021) Re-recognizing micro locations of nanoscale zero-valent iron in biochar using C-TEM technique. *Sci Rep* 11:5037. <https://doi.org/10.1038/s41598-021-84685-w>
- Yang L, Shen J, Zhang W, Wu W, Wei Z, Chen M, Yan J, Qian L, Han L, Li J, Gu M (2022) Hydrothermally assisted synthesis of nano zero-valent iron encapsulated in biomass-derived carbon for peroxymonosulfate activation: the performance and mechanisms for efficient degradation of monochlorobenzene. *Sci Total Environ* 829:154645. <https://doi.org/10.1016/j.scitotenv.2022.154645>
- Zhang X, Yan Q, Li J, Chu I-W, Toghiani H, Cai Z, Zhang J (2018a) Carbon-based nanomaterials from biopolymer lignin via catalytic thermal treatment at 700 to 1000 °C. *Polymers* 10:183. <https://doi.org/10.3390/polym10020183>
- Zhang X, Yan Q, Li J, Zhang J, Cai Z (2018b) Effects of physical and chemical states of iron-based catalysts on formation of carbon-encapsulated iron nanoparticles from kraft lignin. *Materials* 11:139. <https://doi.org/10.3390/ma11010139>
- Zhang C, Tang J, Gao F, Yu C, Li S, Lyu H, Sun H (2021a) Tetrahydrofuran aided self-assembly synthesis of nZVI@gBC composite as persulfate activator for degradation of 2,4-dichlorophenol. *Chem Eng J*. <https://doi.org/10.1016/j.cej.2021.134063>
- Zhang X, Navarathna CM, Leng W, Karunaratne T, Thirumalai RVKG, Kim Y, Pittman CU Jr, Mlsna T, Cai Z, Zhang J (2021b) Lignin-based few-layered graphene-encapsulated iron nanoparticles for water remediation. *Chem Eng J* 417:129199. <https://doi.org/10.1016/j.cej.2021.129199>
- Zhang X, Elsayed I, Nayanathara RMO, Song X, Shmulsky R, Hassan EB (2022a) Biobased hierarchically porous carbon featuring micron-sized honeycomb architecture for CO<sub>2</sub> capture and water remediation. *J Environ Chem Eng* 10:107460. <https://doi.org/10.1016/j.jece.2022.107460>
- Zhang X, Karunaratne T, Navarathna C, Zhang J, Pittman CU (2022b) Nanoscale zero-valent iron-decorated biochar for aqueous contaminant removal. In: Mohan D, Pittman CU Jr, Mlsna TE (eds) *Sustainable biochar for water and wastewater treatment*. Elsevier, Amsterdam, pp 611–641. <https://doi.org/10.1016/B978-0-12-822225-6.00001-4>
- Zhou Y, Gao B, Zimmerman AR, Cao X (2014) Biochar-supported zerovalent iron reclaims silver from aqueous solution to form antimicrobial nanocomposite. *Chemosphere* 117:801–805. <https://doi.org/10.1016/j.chemosphere.2014.10.057>
- Zhu S, Ho S-H, Huang X, Wang D, Yang F, Wang L, Wang C, Cao X, Ma F (2017) Magnetic nanoscale zerovalent iron assisted biochar: interfacial chemical behaviors and heavy metals remediation performance. *ACS Sustain Chem Eng* 5:9673–9682. <https://doi.org/10.1021/acssuschemeng.7b00542>
- Zhuo S-N, Ren H-Y, Cao G-L, Xie G-J, Xing D-F, Ren N-Q, Liu B-F (2022) Highly efficient activation of persulfate by encapsulated nano-Fe<sup>0</sup> biochar for acetaminophen degradation: rich electron environment and dominant effect of superoxide radical. *Chem Eng J* 440:135947. <https://doi.org/10.1016/j.cej.2022.135947>

Submit your manuscript to a SpringerOpen® journal and benefit from:

- Convenient online submission
- Rigorous peer review
- Open access: articles freely available online
- High visibility within the field
- Retaining the copyright to your article

Submit your next manuscript at ► [springeropen.com](https://www.springeropen.com)